

¹ RESEARCH

² **Modelling the cell-type specific mesoscale murine connectome with
3 anterograde tracing experiments**

⁴ **Samson Koelle**^{1,2}, **Dana Mastrovito**¹, **Jennifer D Whitesell**¹, **Karla E Hirokawa**¹, **Hongkui Zeng**¹, **Marina Meila**², **Julie A
5 Harris**¹, **Stefan Mihalas**¹

⁶ ¹ Allen Institute for Brain Science, Seattle, WA, USA

⁷ ²Department of Statistics, University of Washington, Seattle, WA, USA

⁸ **Keywords:** [Connectivity, Cell-type, Mouse]

ABSTRACT

⁹ The Allen Mouse Brain Connectivity Atlas consists of anterograde tracing experiments targeting
¹⁰ diverse structures and classes of projecting neurons. Beyond regional anterograde tracing done in
¹¹ C57BL/6 wild type mice, a large fraction of experiments are performed using transgenic Cre-lines.
¹² This allows access to cell-class specific whole brain connectivity information, with class defined by
¹³ the transgenic lines. However, even though the number of experiments is large, it does not come close
¹⁴ to covering all existing cell classes in every area where they exist. Here, we study how much we can fill
¹⁵ in these gaps and estimate the cell-class specific connectivity function given the simplifying
¹⁶ assumptions that nearby voxels have smoothly varying projections, but that these projection tensors
¹⁷ can change sharply depending on the region and class of the projecting cells.

¹⁸ This paper describes the conversion of Cre-line tracer experiments into class-specific connectivity
¹⁹ matrices representing the connection strengths between source and target structures. We introduce
²⁰ and validate a novel statistical model for creation of connectivity matrices. We extend the

21 Nadaraya-Watson kernel learning method which we previously used to fill in spatial gaps to also fill in
22 a gaps in cell-class connectivity information. To do this, we construct a "cell-class space" based on
23 class-specific averaged regionalized projections and combine smoothing in 3D space as well as in this
24 abstract space to share information between similar neuron classes. Using this method we construct a
25 set of connectivity matrices using multiple levels of resolution at which discontinuities in connectivity
26 are assumed. We show that the connectivities obtained from this model display expected cell-type
27 and structure specific connectivities. We also show that the wild type connectivity matrix can be
28 factored using a sparse set of factors, and analyze the informativeness of this latent variable model.

AUTHOR SUMMARY

29 Large-scale studies have described the connections between areas in multiple mammalian models in
30 ever expanding detail. Standard connectivity studies focus on the connection strength between areas.
31 However, when describing functions at a local circuit level, there is an increasing focus on cell types.
32 We have recently described the importance of connection types in the cortico-thalamic system, which
33 allows an unsupervised discovery of its hierarchical organization. In this study we focus on adding a
34 dimension of connection type for a brain-wide mesoscopic connectivity model. Even with our
35 relatively massive dataset, the data in the cell type direction for connectivity is quite sparse, and we
36 had to develop methods to more reliably extrapolate in such directions, and to estimate when such
37 extrapolations are impossible. This allows us to fill in such a connection type specific inter-areal
38 connectivity matrix to the extent our data allows. While analyzing this complex connectivity, we
39 observed that it can be described via a small set of factors. While not complete, this connectivity
40 matrix represents a a categorical and quantitative improvement in mouse mesoscale connectivity
41 models.

1 INTRODUCTION

42 The mammalian nervous system enables an extraordinary range of natural behaviors, and has
43 inspired much of modern artificial intelligence. Neural connections from one region to another form
44 the architecture underlying this capability. These connectivities vary by neuron type, as well as source
45 cell body location and target axonal projection structures. Thus, characterization of the relationship
46 between neuron type and source and target structure is important for understanding the overall
47 nervous system.

48 Viral tracing experiments - in which a viral vector expressing GFP is transduced into neural cells
49 through stereotaxic injection - are a useful tool for mapping these connections on the mesoscale
50 (Chamberlin, Du, de Lacalle, & Saper, 1998; Daigle et al., 2018; J. A. Harris, Oh, & Zeng, 2012). The GFP
51 protein moves into the axon of the projecting neurons. The long range connections between different
52 areas are generally formed by axons which travel from one region to another. Two-photon
53 tomography imaging can be used to determine the location and strength of the fluorescent signals in
54 two-dimensional slices. These locations can then be mapped back into three-dimensional space, and
55 the signal may then be integrated over area into cubic voxels to give a finely-quantized
56 three-dimensional fluorescence.

57 Several statistical models for the conversion of such experiment-specific signals into generalized
58 estimates of connectivity strength have been proposed (K. D. Harris, Mihalas, & Shea-Brown, 2016;
59 Knox et al., 2019; Oh et al., 2014; ?). Of these, Oh et al. (2014) and Knox et al. (2019) model **regionalized**
60 **connectivities**, which are voxel connectivities integrated by region. The value of these models is that
61 they provide some improvement over simply averaging the projection signals of injections in a given
62 region. However, these previous works only model connectivities observed in wild type mice in which
63 all neuron types were labeled, and so are poorly suited for extension to tracing experiments that
64 induce cell-type specific fluorescence (J. A. Harris et al., 2019). In particular, GFP expression is
65 induced by Cre-recombinase in cell-types specified by transgenic strain. Thus, this paper introduces a
66 **cell class**-specific statistical model to deal with the diverse set of **Cre-lines** described in J. A. Harris et
67 al. (2019), and expands this model to the entire mouse brain. In cortex a large number of transgenic
68 lines were chosen for their laminar specific expression.

69 Our model is a to-our-knowledge novel estimator that takes into account both the spatial position
70 of the labelled source, as well as the categorical cell class. Like the previously state-of-the-art model in
71 Knox et al. (2019), this model predicts regionalized connectivity as an average over positions within
72 the structure, with nearby experiments given more weight. However, our model weighs class-specific
73 behavior in a particular structure against spatial position, so a nearby experiment specific to a similar
74 cell-class is relatively up-weighted, while a nearby experiment specific to a dissimilar class is
75 down-weighted. This model outperforms the model of Knox et al. (2019) based on its ability to predict
76 held-out experiments in leave-one-out cross-validation. We then use the trained model to estimate
77 overall connectivity matrices for each assayed cell class.

78 The resulting cell-type specific connectivity is a directed weighted multigraph which can be
79 represented as a tensor with missing values. We do not give an exhaustive analysis of this data, but do
80 establish a lower-limit of detection, verify several cell-type specific connectivity patterns found
81 elsewhere in the literature, and show that these cell-type specific signals are behaving in expected
82 ways. We also decompose the wild type connectivity matrix into factors representing archetypal
83 connectivity patterns. These components allow approximation of the regionalized connectivity using
84 a small set of latent components.

85 Section 2 gives information on the data and statistical methodology, and Section 3 presents our
86 results. These include connectivities, assessments of model fit, and subsequent analyses. Additional
87 information on our dataset, methods, and results are given in Supplemental Sections 5, 6, and 7,
88 respectively.

2 METHODS

88 We estimate and analyze cell class-specific connectivity functions using models trained on murine
89 brain viral tracing experiments. This section describes the data used to generate the model, the model
90 itself, the evaluation of the model against its alternatives, and the use of the model in creation of the
91 connectivity estimate matrices. It also includes background on the non-negative matrix factorization
92 method used for decomposing the wild type connectivity matrix into latent factors. Additional
93 information about our data and methods are given in Supplemental Sections 5 and 6, respectively.
94

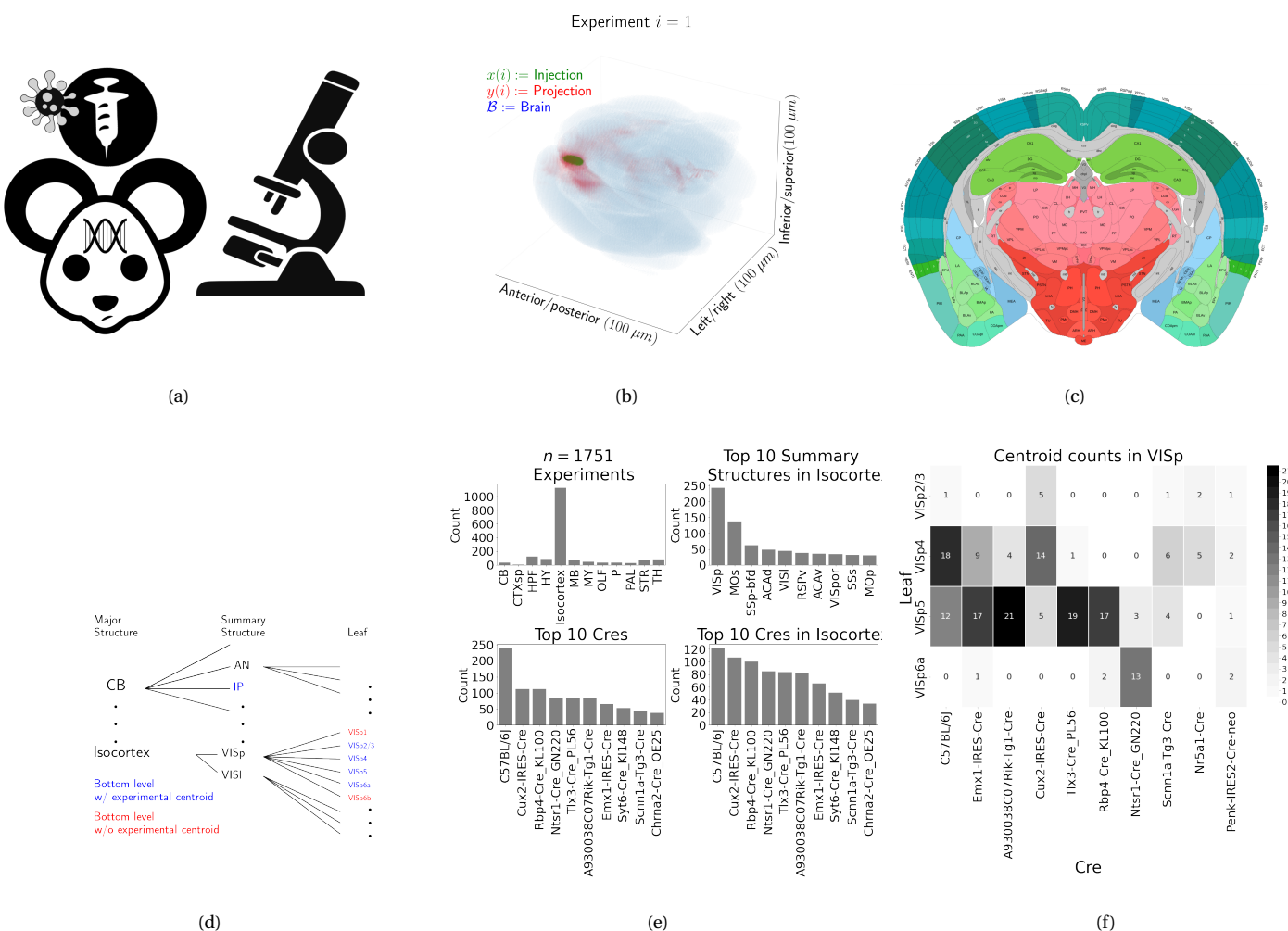


Figure 1: Experimental setting. 1a For each experiment, a Cre-dependent GFP-expressing transgene cassette is transduced by stereotaxic injection into a Cre-driver mouse, followed by serial two-photon tomography imaging. 1b An example of the segmentation of projection (targets) and injection (source) for a single experiment. Within each brain (blue), injection (green) and projection (red) areas are determined via histological analysis and alignment to the Allen Common Coordinate Framework (CCF). 1c Brain region parcellations within a coronal plane of CCFv3. 1d Explanation of nested structural ontology highlighting various levels of CCFv3 structure ontology. Lowest-level (leaf) structures are colored in blue, and structures without an injection centroid are colored in red. 1e Abundances of tracer experiments by Cre-line and region of injection. 1f Co-occurrence of layer-specific centroids and Cre lines within VISp.

95 **Data**

96 Our dataset \mathcal{D} consists of $n = 1751$ publicly available murine brain viral tracing experiments from the
 97 Allen Mouse Brain Connectivity Atlas. Figure 1a summarizes the experimental process used to
 98 generate this data. In each experiment, a mouse is injected with an adeno-associated virus (AAV)
 99 encoding green fluorescent protein (GFP) into a single location in the brain. Location of fluorescence
 100 is mediated by the location of the injection, the characteristics of the transgene, and the genotype of
 101 the mouse. In particular, Cre-driver mice are engineered to express Cre under the control of a specific
 102 and single gene promoter. This localizes expression of Cre to regions with certain transcriptomic
 103 cell-types signatures. In such Cre-driver mice, we used a double-inverted floxed AAV to produce
 104 fluorescence that depends on Cre expression in infected cells. To account for the complex cell-type
 105 targeting induced by a particular combination of Cre-driver genotype and GFP promoter, we refer to
 106 the combinations of cell-types targeted by a particular combination of AAV and Cre-drive mice as
 107 cell-classes. For example, we include experiments from Cre-driver lines that selectively label cell
 108 classes located in distinct cortical layers or other nuclei across the whole brain. By our definition, wild
 109 type mice transduced with constitutively active GFP promoters induce fluorescence of a particularly
 110 broad cell class.

111 For each experiment, the fluorescent signal imaged after injection is aligned into the Allen
 112 Common Coordinate Framework (CCF) v3, a three-dimensional average template brain that is fully
 113 annotated with regional parcellations ?. The whole brain imaging and registration procedures
 114 described in detail in Oh et al. (2014); ? produce quantitative metrics of fluorescence discretized at the
 115 **100 μ m voxel** level. Given an experiment, this image was histologically segmented by an analyst into
 116 *injection* and *projection* areas corresponding to areas containing somas, dendrites and axons or
 117 exclusively axons of the transfected neurons. An example of a single experiment rendered in 3D is
 118 given in Figure 1b. Given an experiment i , we represent injections and projections as functions
 119 $x(i), y(i) : \mathcal{B} \rightarrow \mathbb{R}_{\geq 0}$, where $\mathcal{B} \subset [1 : 132] \times [1 : 80] \times [1 : 104]$ corresponds to the subset of the
 120 $(1.32 \times 0.8 \times 1.04)$ cm rectangular space occupied by the standard voxelized mouse brain. We also
 121 calculate injection centroids $c(i) \in \mathbb{R}^3$ and regionalized projections $y_{\mathcal{T}}(i) \in \mathbb{R}^T$ given by the sum of $y(i)$
 122 in each region. A detailed mathematical description of these steps, including data quality control, is
 123 given in Supplemental Section 6.

124 Our goal is the estimation of **regionalized connectivity** from one region to another. A visual
125 depiction of this region parcellation for a two-dimensional slice of the brain is given in Figure 1c. All
126 structures annotated in the CCF belong to a hierarchically ordered ontology, with different areas of the
127 brain are parcellated to differing finer depths within a hierarchical tree. We denote the main levels of
128 interest as major structures, summary structures, and layers. Not every summary structure has a layer
129 decomposition within this ontology, so we typically consider the finest possible regionalization - for
130 example, layer within the cortex, and summary structure within the thalamus, and denote these
131 structures as leafs. As indicated in Figure 1d, the dataset used to generate the connectivity model
132 reported in this paper contains certain combinations of region and cell class frequently, and others
133 not at all. A summary of the most frequently assayed cell classes and structures is given in Figures 1e
134 and 1f. Since users of the connectivity matrices may be interested in particular combinations, or
135 interested in the amount of data used to generate a particular connectivity estimate, we present this
136 information about all experiments in Supplemental Section 5.

137 ***Modeling Regionalized Connectivity***

Cell-class specific connectivity $f : \mathcal{V} \times \mathbb{R}^3 \times \mathbb{R}^3 \rightarrow \mathbb{R}_{\geq 0}$ gives the directed connection of a particular cell class from one position in the brain to another. In contrast to Knox et al. (2019), which only uses wild type C57BL/6J mice, our dataset has experiments targeting $V = 114$ different combinations of Cre-driver mice and Cre-regulated AAV transgenes jointly denoted as $\mathcal{V} := \{v\}$. As in Knox et al. (2019), we ultimately estimate an integrated regionalized connectivity defined with respect to a set of $S = 564$ source leafs $\mathcal{S} := \{s\}$ and $T = 1123$ target leafs $\mathcal{T} := \{t\}$, of which $1123 - 564 = 559$ are contralateral. That is, we define

$$\text{regionalized connectivity strength } \mathcal{C} : \mathcal{V} \times \mathcal{S} \times \mathcal{T} \rightarrow \mathbb{R}_{\geq 0} \text{ with } \mathcal{C}(v, s, t) = \sum_{l_j \in s} \sum_{l_{j'} \in t} f(v, l_j, l_{j'}),$$

$$\text{normalized regionalized connectivity strength } \mathcal{C}^N : \mathcal{V} \times \mathcal{S} \times \mathcal{T} \rightarrow \mathbb{R}_{\geq 0} \text{ with } \mathcal{C}^N(v, s, t) = \frac{1}{|s|} \mathcal{C}(v, l_j, l_{j'}),$$

$$\text{normalized regionalized projection density } \mathcal{C}^D : \mathcal{V} \times \mathcal{S} \times \mathcal{T} \rightarrow \mathbb{R}_{\geq 0} \text{ with } \mathcal{C}^D(v, s, t) = \frac{1}{|s||t|} \mathcal{C}(v, l_j, l_{j'})$$

138 where l_j and $l_{j'}$ are the locations of source and target voxels, and $|s|$ and $|v|$ are defined to be the
 139 number of voxels in the source and target structure, respectively. Since the normalized strength and
 140 densities are computable from the strength via a fixed normalization, our main statistical goal is to
 141 estimate $\mathcal{C}(v, s, t)$ for all v, s and t . In other words, we want to estimate matrices $\mathcal{C}_v \in \mathbb{R}_{\geq 0}^{S \times T}$. We call this
 142 estimator $\hat{\mathcal{C}}$.

Construction of such an estimator raises the questions of what data to use for estimating which connectivity, how to featurize the dataset, what statistical estimator to use, and how to reconstruct the connectivity using the chosen estimator. We represent these considerations as

$$\hat{\mathcal{C}}(v, s, t) = f^*(\hat{f}(f_*(\mathcal{D}(v, s))). \quad (1)$$

143 This makes explicit the data featurization f_* , statistical estimator \hat{f} , and any potential subsequent
 144 transformation f^* such as summing over the source and target regions. Denoting \mathcal{D} as a function of v
 145 and s reflects that we consider using different data to estimate connectivities for different cell-classes
 146 and source regions. Table 1 reviews estimators used for this data-type used in previous work, as well
 147 as our two main extensions: the Cre-NW and **Expected Loss** (EL) models. Additional information on
 148 these estimators is given in Supplemental Section 6.

Name	f^*	\hat{f}	f_*	$\mathcal{D}(v, s)$
NNLS (Oh et al., 2014)	$\hat{f}(1_s)$	NNLS(X,Y)	$X = x_{\mathcal{S}}, Y = y_{\mathcal{T}}$	I_m/I_m
NW (Knox et al., 2019)	$\sum_{l_s \in s} \hat{f}(l_s)$	NW(X,Y)	$X = l_s, Y = y_{\mathcal{T}}$	I_m/I_m
Cre-NW	$\sum_{l_s \in s} \hat{f}(l_s)$	NW(X,Y)	$X = l_s, Y = y_{\mathcal{T}}$	$(I_l \cap I_v)/I_m$
Expected Loss (EL)	$\sum_{l_s \in s} \hat{f}(s)$	EL(X, Y, v)	$X = l_s, Y = y_{\mathcal{T}}, v$	I_l/I_m

Table 1: Estimation of \mathcal{C} using connectivity data. The regionalization, estimation, and featurization steps are denoted by f^* , \hat{f} , and f_* , respectively. The training data used to fit the model is given by index set I . We denote experiments with centroids in particular major brain divisions and leafs as I_m and I_l , respectively. Data I_l/I_m means that, given a location $l_s \in s \in m$, the model \hat{f} is trained on all of I_m , but only uses I_l for prediction. The non-negative least squares estimator (NNLS) fits a linear model that predicts regionalized projection signal $y_{\mathcal{T}}$ as a function of regionalized injection signal $x_{\mathcal{S}}$. Thus, the regionalization step for a region s is given by applying the learned matrix \hat{f} to the s -th indicator vector. In contrast, the Nadaraya-Watson model (NW) is a local smoothing model that generates a prediction for each voxel within the source structure that are then averaged to create estimate the structure-specific connectivity.

149 Our contributions - the Cre-NW and Expected Loss (EL) models - have several differences from the
 150 previous methods. In contrast to the non-negative least squares (Oh et al., 2014) and
 151 Nadaraya-Watson (Knox et al., 2019) estimators that account only for source region s , our new
 152 estimators account cell class v . The Cre-NW estimator only uses experiments from a particular class
 153 to predict connectivity for that class, while the EL estimator shares information between classes
 154 within a structure. Both of these estimator take into account both the cell-class and the centroid
 155 position of the experimental injection. Like the NW and Cre-NW estimator, the EL estimator
 156 generates predictions for each voxel in a structure, and then sums them together to get the overall
 157 connectivity. However, in contrast to the NW approaches, the EL estimate of the projection vector for
 158 a cell-class at a location weights the average projection of that cell-class in the region containing the
 159 location against the relative locations of all experimental centroids in the region regardless of class.

¹⁶⁰ That is, cell-class and source region combinations with similar average projection vectors will be
¹⁶¹ upweighted when estimating \hat{f} . Thus, all experiments that are nearby in three-dimensional space can
¹⁶² help generate the prediction, even when there are few nearby experiments for the cell-class in
¹⁶³ question. A detailed mathematical description of our new estimator is given in Supplemental Section
¹⁶⁴ 6. (SK's comment:**cell-class versus Cre-line?**)

165 ***Model evaluation***

166 We select optimum functions from within and between our estimator classes using **leave-one-out**
 167 **cross validation**, in which the accuracy of the model is assessed by its ability to predict experiments
 168 excluded from the training data. Equation 1 includes a deterministic step f^* included without input
 169 by the data. The performance of $\widehat{\mathcal{C}}(v, s, t)$ is thus determined by performance of $\widehat{f}(f_*(\mathcal{D}(v, s)))$. Thus,
 170 we evaluate prediction of $f_{\mathcal{T}} : \mathbb{R}^3 \rightarrow \mathbb{R}_{\geq 0}^T$ - the regionalized connection strength at a given location.

171 Another question is what combinations of v , s , and t to generate a prediction for. Our EL and
 172 Cre-NW models are leaf specific. They only generate predictions for cell-classes in leafs where at least
 173 one experiment with a Cre-line targeting that class has a centroid. To accurately compare our new
 174 estimators with less-restrictive models such as used in Knox et al. (2019), we restrict our evaluation set
 175 to Cre driver/leaf combinations that are present at least twice. The sizes of these evaluation sets are
 176 given in Supplemental Section 5.

We use weighted $l2$ -loss to evaluate these predictions.

$$\text{l2-loss } \ell(y_{\mathcal{T}}(i)), \widehat{y_{\mathcal{T}}(i)}) := \|y_{\mathcal{T}}(i)) - \widehat{y_{\mathcal{T}}(i)}\|_2^2.$$

$$\text{weighted l2-loss } \mathcal{L}(\widehat{f}(f_*)) := \frac{1}{|\{\mathcal{S}, \mathcal{V}\}|} \sum_{s, v \in \{\mathcal{S}, \mathcal{V}\}} \frac{1}{|I_s \cap I_v|} \sum_{i \in (I_s \cap I_v)} \ell(y_{\mathcal{T}}(i)), \widehat{f}_{\mathcal{T}}(f_*(\mathcal{D}(v, s) \setminus i)).$$

177 This is a somewhat different loss from Knox et al. (2019), both because of the normalization of
 178 projection, and because of the increased weighting of rarer combinations of s and v implicit in the
 179 $\frac{1}{|I_s \cap I_v|}$ term in the loss. The establishment of a lower limit of detection and the extra cross-validation
 180 step used in the EL model to establish the relative importance of regionally averaged cell-class
 181 projection and injection centroid position are covered in Supplemental Section 6.

182 ***Connectivity analyses***

183 We examine latent structure underlying our estimated connectome using two types of unsupervised
 184 learning. Our use of hierarchical clustering is standard, and so we do not review it here. However, our
 185 application of non-negative matrix factorization (NMF) to decompose the estimated long-range
 186 connectivity into **connectivity archetypes** that linearly combine to reproduce the observed
 187 connectivity of some independent interest. Non-negative matrix factorization refers to a collection of
 188 **dictionary-learning** algorithms for decomposing a non-negatively-valued matrix such as \mathcal{C} into
 189 positively-valued matrices called, by convention, weights $W \in \mathbb{R}_{\geq 0}^{S \times q}$ and hidden units $H \in \mathbb{R}_{\geq 0}^{q \times T}$.
 190 Unlike PCA, NMF specifically accounts for the fact that data are all in the positive orthant. The matrix
 191 H is typically used to identify latent structures with interpretable biological meaning, and the choice
 192 of matrix factorization method reflects particular scientific subquestions and probabilistic
 193 interpretations.

194 Our algorithm solves the following optimization problem

$$\text{NMF}(\mathcal{C}, \lambda, q) := \arg \min_{W \in \mathbb{R}_{\geq 0}^{S \times q}, H \in \mathbb{R}_{\geq 0}^{q \times T}} \frac{1}{2} \| \mathbf{1}_{d(s,t) > 1500\mu m} \odot \mathcal{C} - WH \|_2^2 + \lambda (\|H\|_1 + \|W\|_1).$$

195 For this decomposition we ignore connections between source and target regions less than $1500\mu m$
 196 apart. This is because short-range projections resulting from diffusion dominate the matrices $\hat{\mathcal{C}}$, and
 197 represent a less-interesting type of biological structure. We set $\lambda = 0.002$ to encourage sparser and
 198 therefore more interpretable components. We use unsupervised cross-validation to determine an
 199 optimum q , and show the top 15 stable components (?). Stability analysis accounts for the
 200 difficult-to-optimize NMF program by clustering the resultant H from multiple replicates. Since the
 201 NMF objective is difficult to optimize and sensitive to initialization, we follow up with a stability
 202 analysis. The medians of the component clusters appearing frequently across NMF replicates are
 203 selected as **connectivity archetypes**. Details of these approaches are given in Supplementary Sections
 204 6 and 7.

3 RESULTS

²⁰⁵ We provide several types of results. First, we show that the novel expected-loss (EL) estimator
²⁰⁶ performs best in our validation assays. Second, qualitative exploratory analysis confirms that the
²⁰⁷ Cre-specific connectivity matrices generated using this model are consistent with known biology.
²⁰⁸ Third, statistical decomposition of the wild-type connectivity matrix using unsupervised learning
²⁰⁹ shows how archetypal components can combine to produce observed signals.

²¹⁰ ***Model evaluation***

²¹¹ Our EL model generally performs better than the other estimators that we consider. Table 5 contains
²¹² weighted losses from leave-one-out cross-validation of candidate models, such as the NW Major-WT
²¹³ model from Knox et al. (2019). The EL model combines the good performance of class-specific
²¹⁴ models like NW Leaf-Cre in regions like Isocortex with the good performance of class-agnostic models
²¹⁵ in regions like Thalamus. Additional information on model evaluation, including class and structure-
²¹⁶ specific performance, is given in Appendix 5. In particular, Supplementary Table 4 contains the sizes
²¹⁷ of these evaluation sets in each major structure, and Supplementary Section 7 contains the structure-
²¹⁸ and class specific losses.

	Mean Leaf-Cre	NW Major-Cre	NW Leaf-Cre	NW Leaf	NW Major-WT	NW Major	EL
\hat{f}	Mean	NW	NW	NW	NW	NW	EL
\mathcal{D}	$I_c \cap I_L$	$I_c \cap I_M$	$I_c \cap I_L$	I_L	$I_{wt} \cap I_M$	I_M	I_L
Isocortex	0.239	0.252	0.234	0.279	0.274	0.274	0.228
OLF	0.193	0.233	0.191	0.135	0.179	0.179	0.138
HPF	0.175	0.332	0.170	0.205	0.228	0.228	0.153
CTXsp	0.621	0.621	0.621	0.621	0.621	0.621	0.621
STR	0.131	0.121	0.128	0.169	0.232	0.232	0.124
PAL	0.203	0.205	0.203	0.295	0.291	0.291	0.188
TH	0.673	0.664	0.673	0.358	0.379	0.379	0.369
HY	0.360	0.382	0.353	0.337	0.317	0.317	0.311
MB	0.168	0.191	0.160	0.199	0.202	0.202	0.159
P	0.292	0.292	0.292	0.299	0.299	0.299	0.287
MY	0.268	0.347	0.268	0.190	0.189	0.189	0.204
CB	0.062	0.062	0.062	0.068	0.112	0.112	0.068

Table 2: Losses from leave-one-out cross-validation of candidate models. **Bold** numbers are best for their major structure.

219 ***Connectivities***

220 Our main result is the estimation of matrices $\hat{\mathcal{C}}_v \in \mathbb{R}_{\geq 0}^{S \times T}$ representing connections of source structures
 221 to target structures for particular cre-lines v . We confirm the detection of several well-established
 222 connectivities within our tensor, although it is our expectation that additional interesting biological
 223 processes are also manifest. The connectivity tensor and code to reproduce it are available at
 224 https://github.com/AllenInstitute/mouse_connectivity_models/tree/2020.

225 *Overall connectivity* Several expected biological projection patterns are evident in the wild-type
 226 connectivity matrix \mathcal{C}_{wt} from leaf sources to leaf targets shown in Figure 2a. Intraareal connectivities
 227 are clear, as are ipsilateral connections between cortex and thalamus. The clear intrastructural and
 228 intraareal connectivities mirror previous estimates in Oh et al. (2014) and Knox et al. (2019) and
 229 descriptive depictions of individual experiments in J. A. Harris et al. (2019).

230 Our estimated wild-type connectivities appear more variable than those in Knox et al. (2019), which
 231 used the NW Major-WT model whose accuracy is evaluated in Table 5. This is plausibly because of
 232 both the layer-specific targeting of the different cre-lines, and also the layer-specificity of the selected
 233 model. Although layer-specificity is a major advantage of including distinct cre-lines, for comparison,
 234 we also plot coarser projections between summary-structure sources and targets in the cortex in
 235 Figure 2b. These are averages over component layers weighted by layer size. Grossly congruent with
 236 the previous work, these results also exhibit a larger range of connectivities than those in Knox et al.
 237 (2019). Importantly, as shown in Table 5 this finer spatial resolution corresponds to the increased
 238 accuracy of our EL model over the NW Major-WT model.

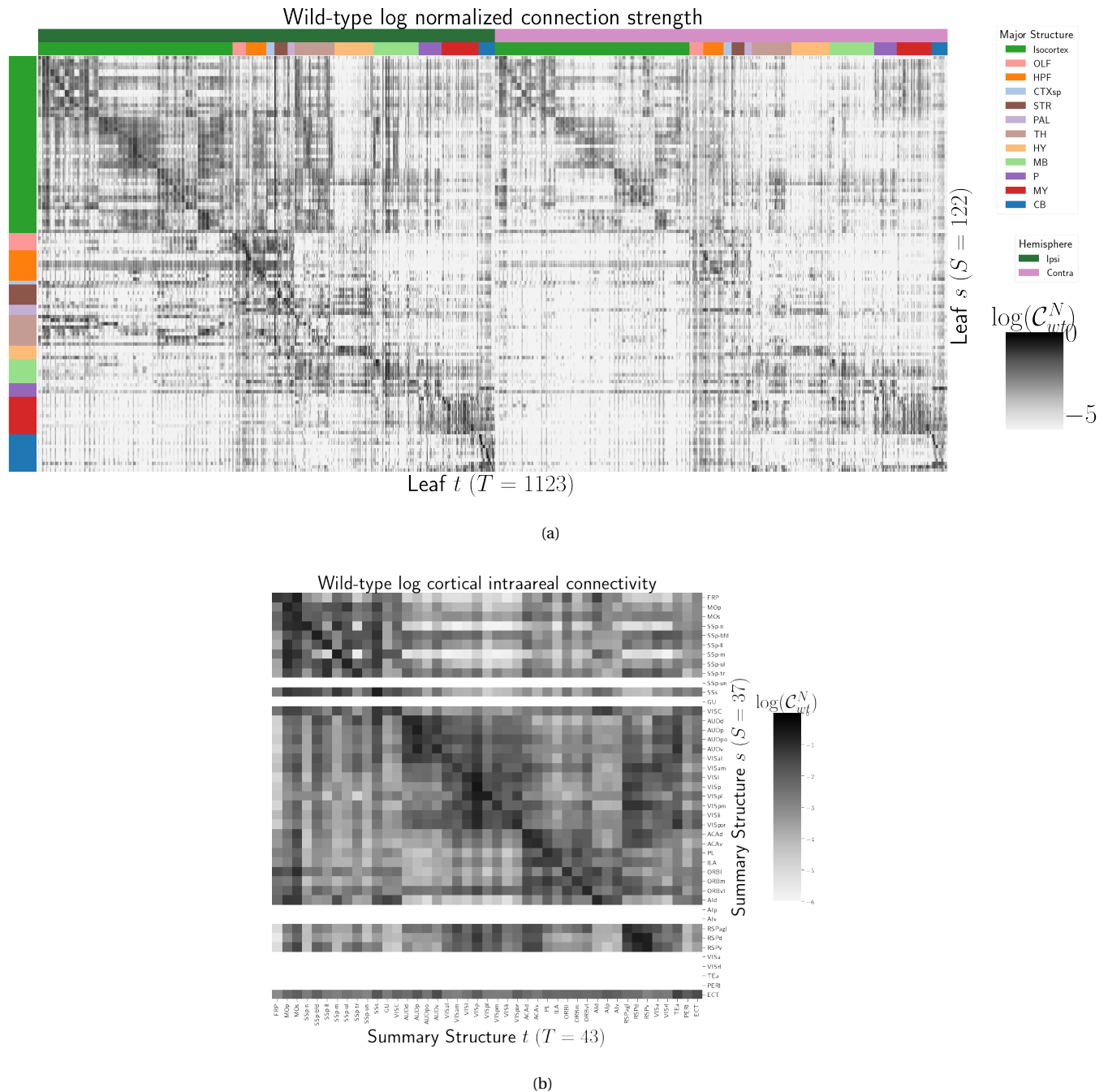


Figure 2: Wild-type connectivities. 2a Log wild-type connectivity matrix $\log \mathcal{C}(s, t, v_{wt})$. 2b Log wild-type intracortical connectivity matrix at the summary structure level.

239 *Class-specific connectivities* Source and cell-type combinations which project similarly indicate the
 240 network structure underpinning cognition. Although there is a rich anatomical literature using
 241 anterograde tracing data to describe projection patterns from subcortical sources to a small set of
 242 targets of interest, most accessible whole brain projection data are from the Allen Mouse Connectivity
 243 Atlas (MCA) project used here to generate the connectome models. Thus, to validate our results while
 244 avoiding a circular validation of the data used to generate the model weights, we confirm that these
 245 class-specific connectivities exhibit certain known behaviors. In particular, we focus on several cell
 246 types and source areas with extensive previous anatomical descriptions of projections using both bulk
 247 tracer methods with cell type specificity and single cell reconstructions: 1) thalamic-projecting
 248 neurons in the visual and motor cortical regions, 2) cholinergic neurons in the medial septum and
 249 nucleus of the diagonal band (MS/NDB); 3) cholinergic neurons in the caudoputamen, and 4)
 250 serotonergic neurons of the dorsal raphe nucleus (DR). We find that our inferred connections are in
 251 agreement with literature on these cell types.

252 DEPENDENCE OF THALAMIC CONNECTION ON CORTICAL LAYER. Visual cortical areas VISp and VISl and
 253 cortical motor areas MOp and MOs are ideal testbeds for our connectivities because there are
 254 well-established layer-specific projection patterns that can be labeled with the layer-specific cre-lines
 255 from the Allen datasets and others J. A. Harris et al. (2019); Jeong et al. (2016), and are also
 256 well-represented in our dataset. Figure 3a shows that in VISp, the Ntsr1-Cre line strongly targets the
 257 core part of the thalamic LGd nucleus while in VISl has a very strong projection to the LP nucleus. In
 258 VISp, the the Rbp-4Cre strongly targets LP as well. Recall that we display connectivity estimates for
 259 structures with at least one injection centroid in the structure. Thus, the position of non-zero rows in
 260 Figure 3a shows the localization of Rbp4-Cre and Ntsr1-Cre injection centroids to layers 5 and 6
 261 respectively. This is further examined in Supplemental Section ??). Thus, as a heuristic alternative
 262 model, to also synthesize information about leafs targeted by different cre-lines, we also display an
 263 average connectivity matrix over all cre-lines. This combined output is not evaluated in our testing,
 264 and is only a general stand-in for overall behavior, but provides a useful summary of results.

265 MS AND NDB PROJECTIONS IN THE CHAT-IRES-CRE-NEO MODEL. Cholinergic neurons in the MS and
 266 NDB are well-known to strongly innervate the hippocampus, olfactory bulb, piriform cortex,
 267 entorhinal cortex, and lateral hypothalamus (Watson, Paxinos, & Puelles, 2012; Zaborszky et al., 2015).

268 In the Allen MCA, cholinergic neurons were labeled by injections into Chat-IRES-Cre-neo mice. We
 269 first checked the estimated connectome weights to targets in these major brain divisions from MS and
 270 NDB. We observed that all these expected divisions were represented above the 90th percentile of
 271 weights. Recently, a single cell whole brain mapping project using Chat-Cre mice fully reconstructed
 272 n=50 cells, revealing these same major targets and also naming additional targets from MS/NDB (Li et
 273 al., 2018). We compared our Chat-IRES-Cre connectome model data for MS and NDB with the targets
 274 identified by Li et al. (2018). We identified 150 targets at the fine leaf structure level in the top 10% of
 275 estimated weights. To directly compare our data across studies, we had to merge structures as needed
 276 to get to the same ontology level and remove ipsilateral and contralateral information. After
 277 formatting our data, we found 51 targets in the top 10%; Li et al. reported 47 targets across the 50 cells.
 278 There was good consistency overall between the target sets; 35 targets were shared, 12 were unique to
 279 the single cell dataset, and 16 unique to our model data. We checked whether targets missing from
 280 our dataset were because of the threshold level. Indeed, lowering the threshold to the 75 th percentile
 281 confirmed 6 more targets-in-common, and all but 2 targets from Li et al. (2018) were above the 50th
 282 percentile weights in our model. Of note, the absence of a target in the single cell dataset that was
 283 identified in our model data is most likely due to the sparse sampling of all possible projections from
 284 only n=50 MS/NDB cells.

285 CP PROJECTIONS IN THE CHAT-IRES-CRE-NEO MODEL. Most cells in the caudoputamen (CP) are
 286 GABAergic spiny projection neurons. These cells are also the only type that send projections outside
 287 the CP. Cholinergic interneurons make up 1-2% of all CP cells and their axon terminals do not extend
 288 beyond the CP borders. We confirmed that the model predictions for connection weights from CP
 289 cholinergic cells were consistent with this known anatomy; the connection weight to CP was ~ 2-fold
 290 higher than any other in the top 5%.

291 DR PROJECTIONS IN THE SLC6A4-CRE'ET33 MODEL. Serotonergic projections from cells in the
 292 dorsal raphe (DR) are widely distributed and innervate many forebrain structures including isocortex
 293 and amygdala. In the Allen MCA, serotonergic neurons were labeled using Slc6a4-Cre_ET33 and
 294 Slc6a4-CreERT2_EZ13 mice. This small nucleus appears to contain a complex mix of molecularly
 295 distinct serotonergic neuron subtypes with some hints of subtype-specific projection patterns (Huang
 296 et al., 2019; Ren et al., 2018, 2019). We expect that the Cre lines we used here in the Allen MCA, which

297 utilize the serotonin transporter promoter (*Slc6a4-Cre* and *-CreERT2*), will lead to expression of tracer
298 in all the serotonergic subtypes recently described in an unbiased way, but this assumption has not
299 been tested directly. We compared our model data to a single cell reconstruction dataset consisting of
300 n=50 serotonergic cells with somas in the DR that also had bulk tracer validation (SK's
301 **comment:INSERT LINK TO FIGURE**). Ren et al. (2019) listed 55 targets across the single cell
302 reconstructions. After processing our data to match the target structure ontology level across studies,
303 we identified 37 targets from the DR with weights above the 90 th percentile; 27 of these targets
304 matched those named by Ren et al. (2019). Overall there was good consistency between targets in
305 olfactory areas, cortical subplate, CP, ACB and amygdala areas, as well in pallidum and midbrain.

306 The two major brain divisions with the least number of matches are the isocortex and thalamus.
307 There are a few likely reasons for these observations. First, in the isocortex, there is known to be
308 significant variation in the density of projections across different locations, with the strongest
309 innervation in lateral and frontal orbital cortices Ren et al. (2019); ?. Indeed, when we lower the
310 threshold and check for weights of the targets outside of the 90%, we see all but one of these regions
311 (PTLp, parietal cortex which is not frontal or lateral) has a weight assigned in the top half of all targets.
312 In the thalamus, it was also interesting to observe that our model predicted strong connections to
313 several medial thalamic nuclei (i.e., MD, SMT), that were not targeted by the single cells. This
314 discrepancy may be at least partially explained by the complex topographical organization of the DR
315 that, like the molecular subtypes, is not yet completely understood. A previous bulk tracer study that
316 specifically targeted injections to the central, lateral wings, and dorsal subregions of the DR reported
317 semi-quantitative differences in projection patterns (Muzerelle, Scotto-Lomassese, Bernard,
318 Soiza-Reilly, & Gaspar, 2016). Notably, Muzerelle et al. (2016) report that cells in the ventral region of
319 DR project more strongly to medial thalamic nuclei, whereas the lateral and dorsal DR cells innervate
320 more lateral regions (e.g., LGd). So it is possible that the single cell somas did not adequately sample
321 the entire DR.

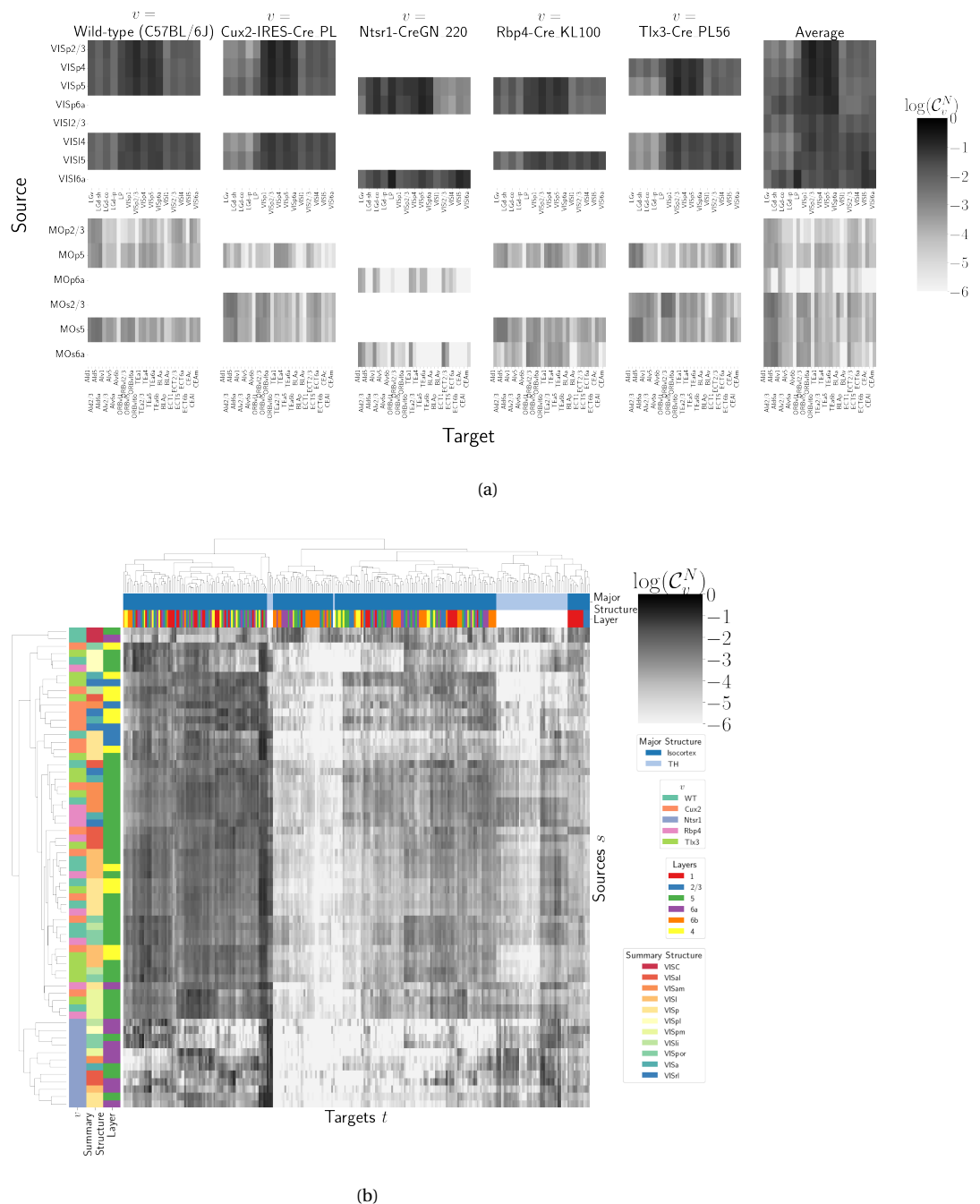


Figure 3: Cell-class specificity. 3a Selected cell-class and layer specific connectivities from two visual and two motor areas. Sources without an injection in the Cre driver line are not estimated due to lack of data for that Cre-line in that structure. 3b Hierarchical clustering of connectivity strengths from visual cortex cell-types to cortical and thalamic targets. Cre-line, summary structure, and layer are labelled on the sources. Major brain division and layer are labelled on the targets.

322 ***Connectivity Analyses***323 **(SK's comment:move to connectivity analysis section)**

324 Cell-class, while often correlated with cortical layer, can be a stronger driver of connectivity than
 325 summary structure especially when looking at targets at major brain division level. Figure 3b shows a
 326 collection of connectivity strengths generated using cre-specific models for wild-type, Cux2, Ntsr1,
 327 Rbp4, and Tlx3 cre-lines from VIS areas at leaf level in the cortex to cortical and thalamic nuclei. We
 328 use hierarchical clustering to sort source structure/cell-class combinations by the similarity of their
 329 structural projections, and sort target structures by the structures from which they receive projections.
 330 Examining the former, we can see that the layer 6 Ntsr1 Cre-line distinctly projects to thalamic nuclei,
 331 regardless of source summary structure. This contrasts with the tendency of other cell-classes to
 332 project intracortically in a manner determined by the source structure. Similarly, layer 6 targets are
 333 not strongly projected to by any of the displayed Cre-lines. There are too many targeted summary
 334 structures to plot here, but we expect that the source profile of each target clusters by structure.

335 Each regionalized connectivity matrix is a high-dimensional realization of relatively few biological
 336 processes, and decomposition of neural signals to recover these processes is a fundamental goal in
 337 neuroscience. In this section, we apply non-negative matrix factorization to decompose the
 338 long-range wild-type connectivities into linear combinations of archetypal connectivities. This
 339 decomposes the remaining censored connectivity matrix into a linear model based off a relatively
 340 small number of distinct signals. This model is able to capture a large amount of the observed
 341 variability, and recovers structure-specific archetypal signals.

342 These signals are plotted in Figure 4, and technical details and intermediate results are given in
 343 Supplemental Sections 6 and 7, respectively. These details include a cross-validation based method
 344 for selecting the number of components, a masking method for focusing only on long range
 345 connections, and a stability method for ensuring that the decomposition is reliable across
 346 computational replicates. The plotted decomposition shows that these underlying connectivity
 347 archetypes correspond strongly to major brain division in both target and sources.

348 Inspection of the reconstructed distal normalized connection strength using the top 15
 349 components shows qualitatively shows that this relatively sparse decomposition is able to capture

350 much of the observed variability. Other connectivity patterns like cortical-cortical and
351 cortical-thalamic are also detected.

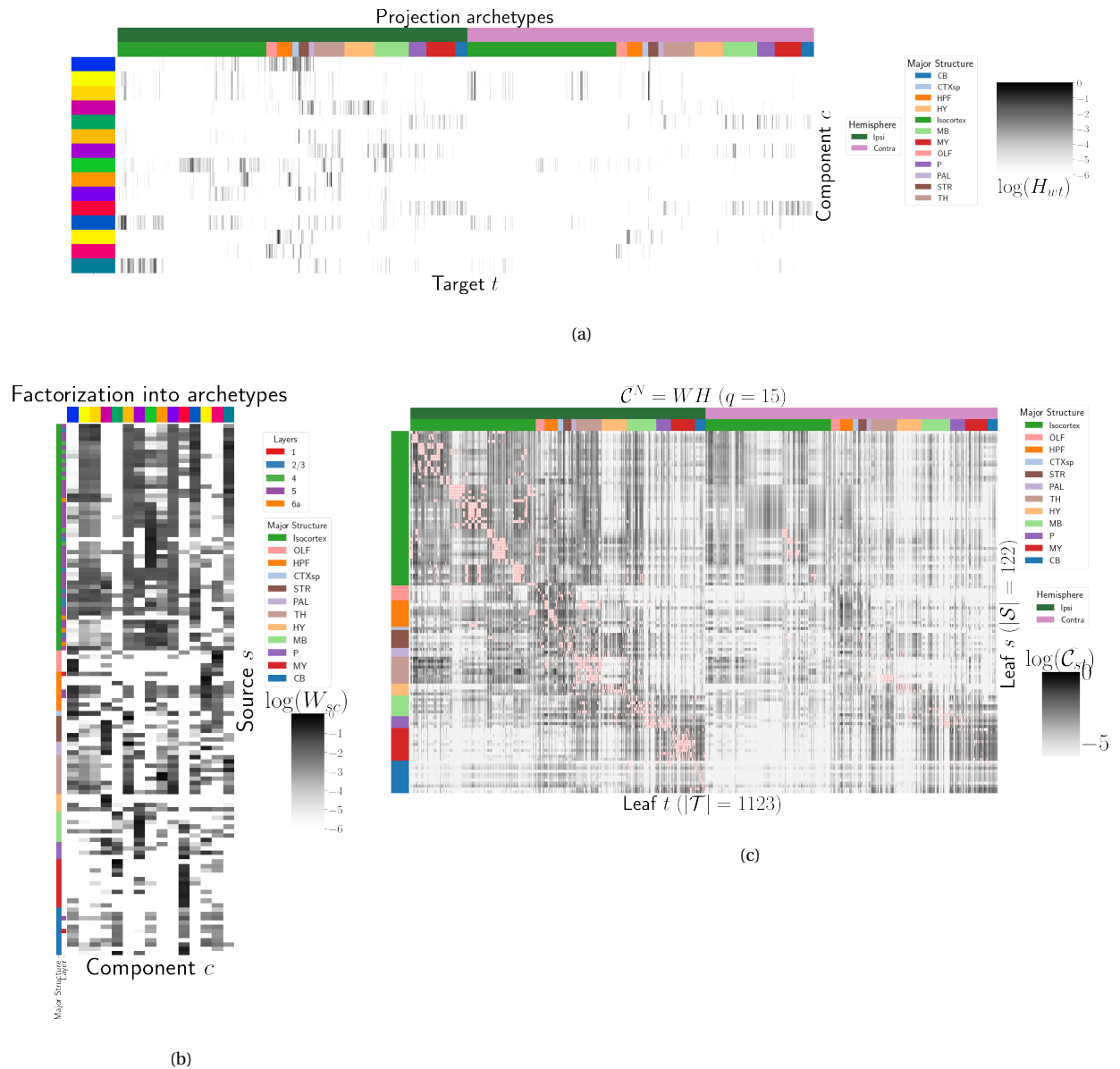


Figure 4: Non-negative matrix factorization results $\mathcal{C}_w^N = W H$ for $q = 15$ components. 4a Latent space coordinates H of \mathcal{C} . Target major structure and hemisphere are plotted. 4b Loading matrix W . Source major structure and layer are plotted. 4c Reconstruction of the normalized distal connectivity strength using the top 15 archetypes. Areas less than $1500 \mu\text{m}$ apart are not modeled, and therefore shown in red.

4 DISCUSSION

352 The model presented here is the first cell-type specific whole brain projectome model for a
 353 mammalian species, and it opens the door for a large number of models linking brain structure to
 354 computational architectures. Overall, we find expected targets, based on our anatomical expertise
 355 and published reports, but underscore that the core utility of this bulk connectivity analysis is not
 356 only in validation of existing connection patterns, but also in identification of new ones. We note that
 357 although the concordance appeared stronger for the cholinergic cells than the serotonergic cells, any
 358 differences might still be explained by the lack of high quality “ground-truth” datasets to validate
 359 these Cre connectome models. Larger numbers of single cell reconstructions, that saturate all
 360 possible projection types, would be a better gold standard than the small number of cells reported
 361 here (n=50 for each). ([SK's comment: add citation](#)) Perhaps future iterations of the connectome model
 362 may also take into account some single cell axon projection data.

363 The Nadaraya-Watson estimator presented here is novel. Beyond using a Nadaraya-Watson kernel
 364 regression defined in physical space, we define a cell-type space based on similarities of projections,
 365 and theoretically justify the use of an intermediate shape-constrained estimator. While methods like
 366 non-negative least squares can also account for covariates, the centroid method from Knox et al.
 367 (2019) was shown that the more precise notion of injection location than the non-negative least
 368 squares in Oh et al. (2014). Furthermore, our sample size seems too low to utilize a fixed or mixed
 369 effect, particularly since the impact of the virus depend on the particular injection region. In a sense
 370 both the NNLS and NW models can be thought of as improvements over the structure-specific
 371 average, and so is also possible that a yet undeveloped residual-based data-driven blend of these
 372 models could provide improved performance.

373 We see several other opportunities for improving on our model. Ours is certainly not the first
 374 cross-validation based model averaging method Gao, Zhang, Wang, and Zou (2016). However, our use
 375 of shape-constrained estimator in target-encoded feature space is novel and fundamentally different
 376 from Nadaraya-Watson estimators that use an optimization method for selecting the weights (Saul &
 377 Roweis, 2003). The properties of this estimator, as well as its relation to estimators fit using an
 378 optimization algorithm, are a possible future avenue of research. A deep model such as Lotfollahi,
 379 Naghipourfar, Theis, and Alexander Wolf (2019) could be appropriate, provided enough data was

380 available. Finally, a Wasserstein-based measure of injection similarity per structure would combine
381 both the physical simplicity of the centroid model while also incorporating the full distribution of the
382 injection signal.

383 The factorization of the connectivity matrix could also be improved and better used. From a
384 statistical perspective, stability-based method for establishing archetypal connectivities in NMF is
385 similar to those applied to genomic data Kotliar et al. (2019); Wu et al. (2016). However, non-linear
386 data transformations or matrix decompositions, or tensor factorizations that account for correlations
387 between cell-types could better capture the true nature of archetypal neural connections. It would
388 also be of great interest to associate the archetypal signals detected from connectivity analysis with
389 undergirding gene expression patterns or functional information.

390 Inspired by how this complexity arises from a relatively parsimonious set of genetic information
391 during development, w Such components can provide a link to the genetic origin of the regionalized
392 connectivity.

ACKNOWLEDGMENTS

³⁹³ We thank the Allen Institute for Brain Science founder, Paul G. Allen, for his vision, encouragement,
³⁹⁴ and support.

395 This supplement is divided into information about our dataset, supplemental methods, and
396 supplemental results. However, certain topics are revisited between sections. Thus, if a reader is
397 interested in, say, non-negative matrix factorization, they may find relevant information in both
398 methods and results.

5 SUPPLEMENTAL INFORMATION

399 Our supplementary information consists of abundances of leaf/Cre-line combinations, information
400 about distances between structures, and the size of our restricted evaluation dataset.

401 *Cre/structure combinations in \mathcal{D}*

402 This section describes the abundances of leaf and Cre-line combinations in our dataset. Users of the
403 connectivity matrices who are interested in a particular Cre-line or structure can see the quantity and
404 type of data used to compute and evaluate that connectivity.

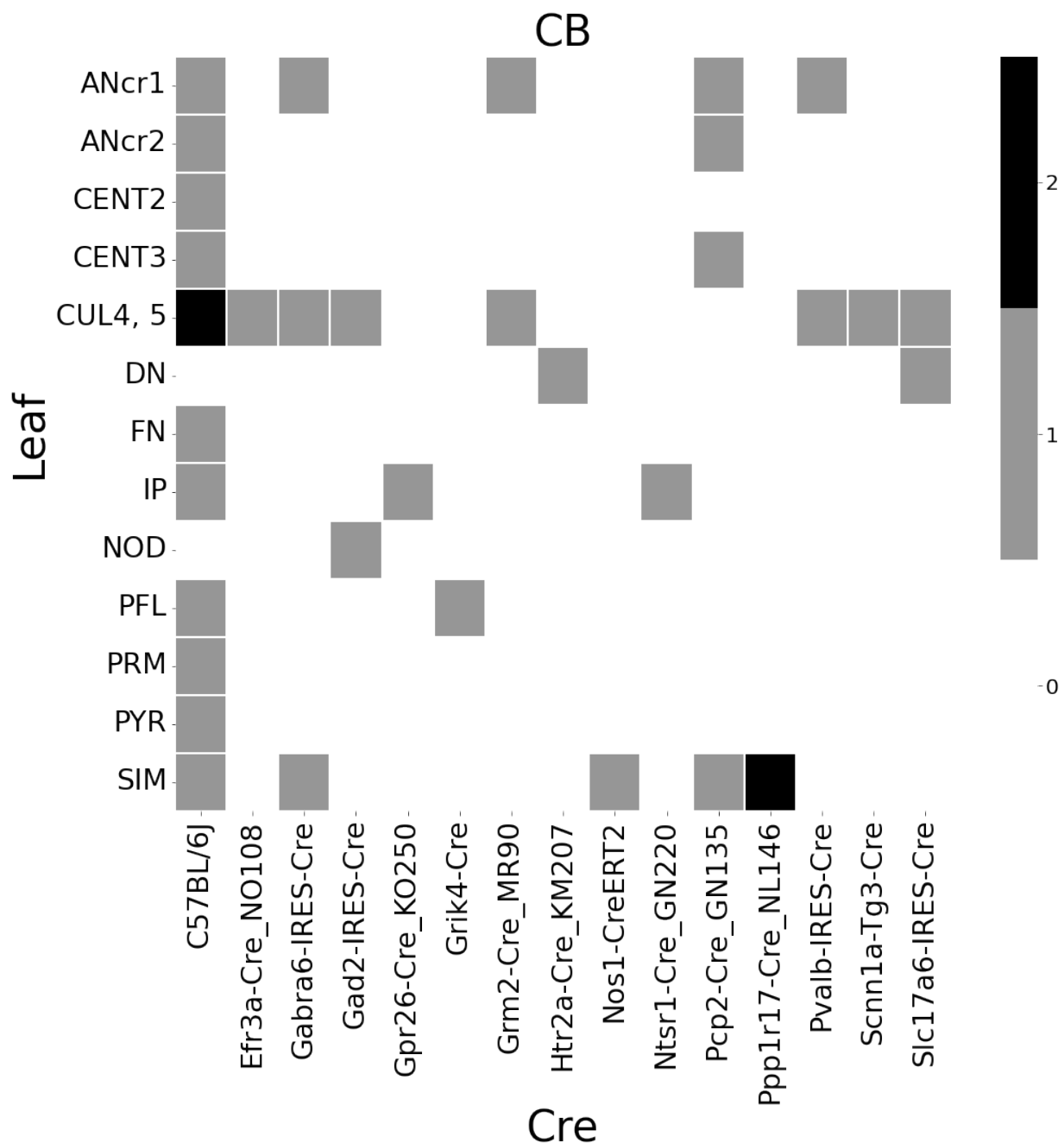


Figure 5: Abundances of Cre-line and leaf-centroid combinations.

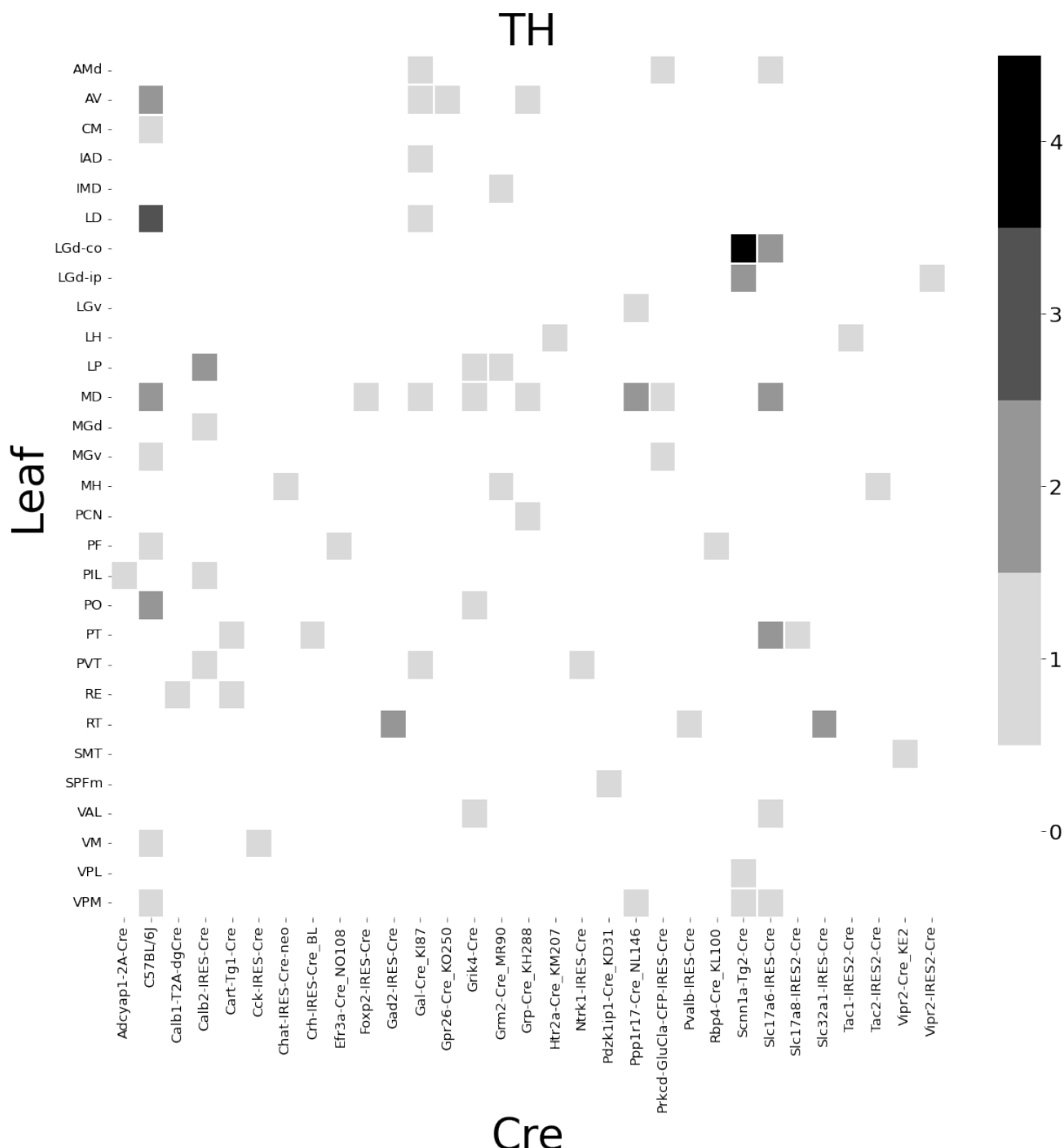


Figure 6: Abundances of Cre-line and leaf-centroid combinations.

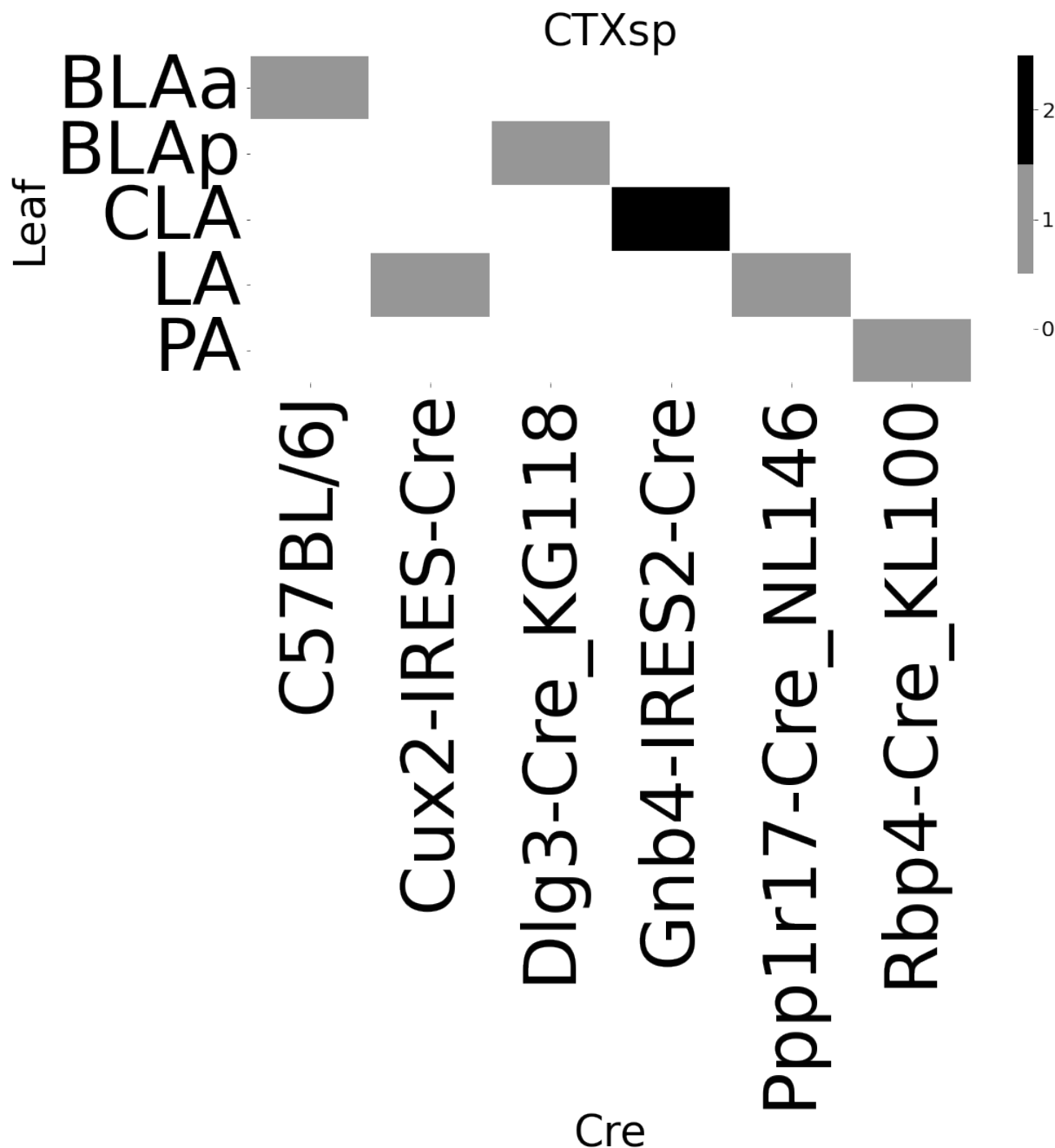


Figure 7: Abundances of Cre-line and leaf-centroid combinations.

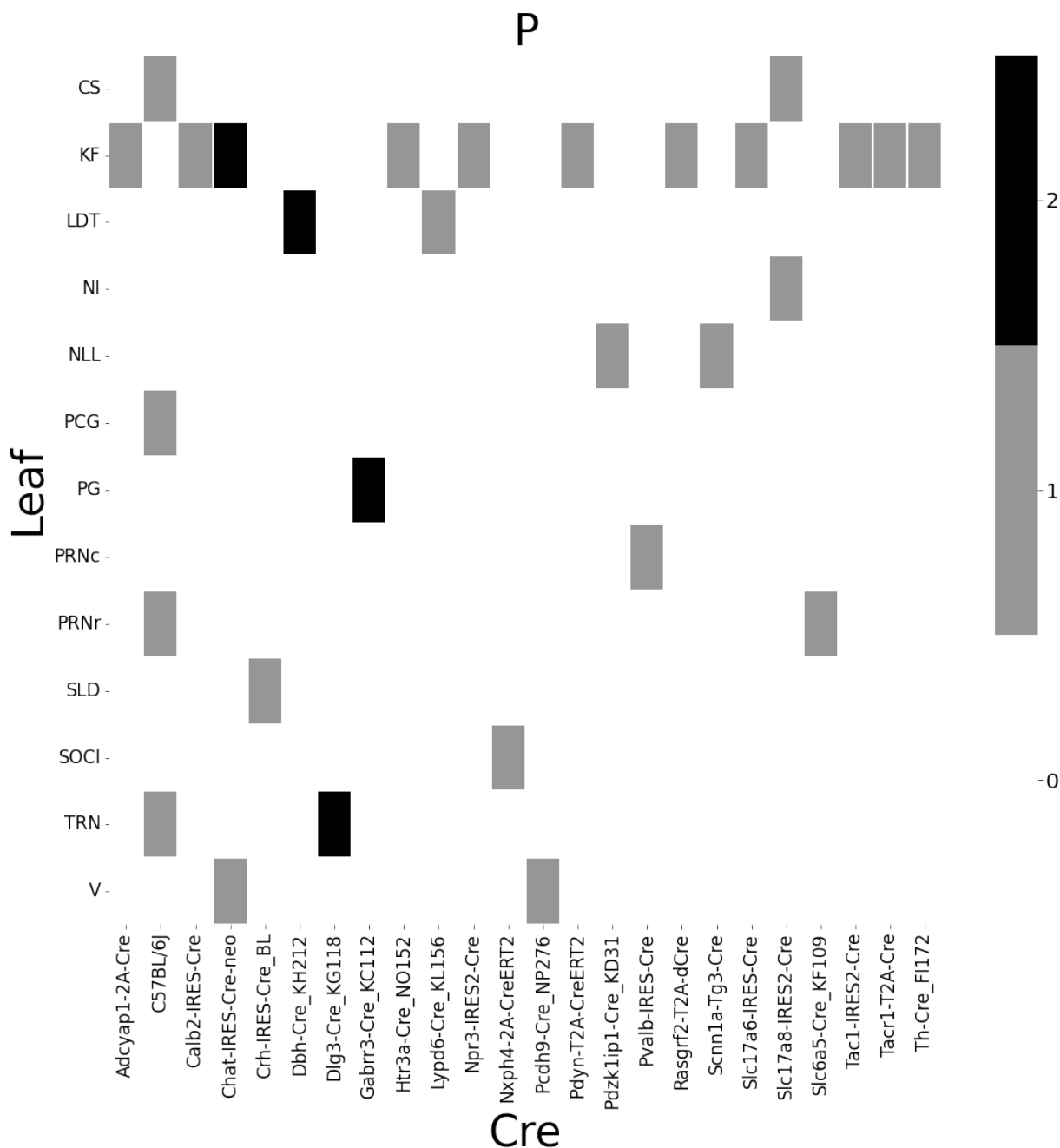


Figure 8: Abundances of cre-line and leaf-centroid combinations.

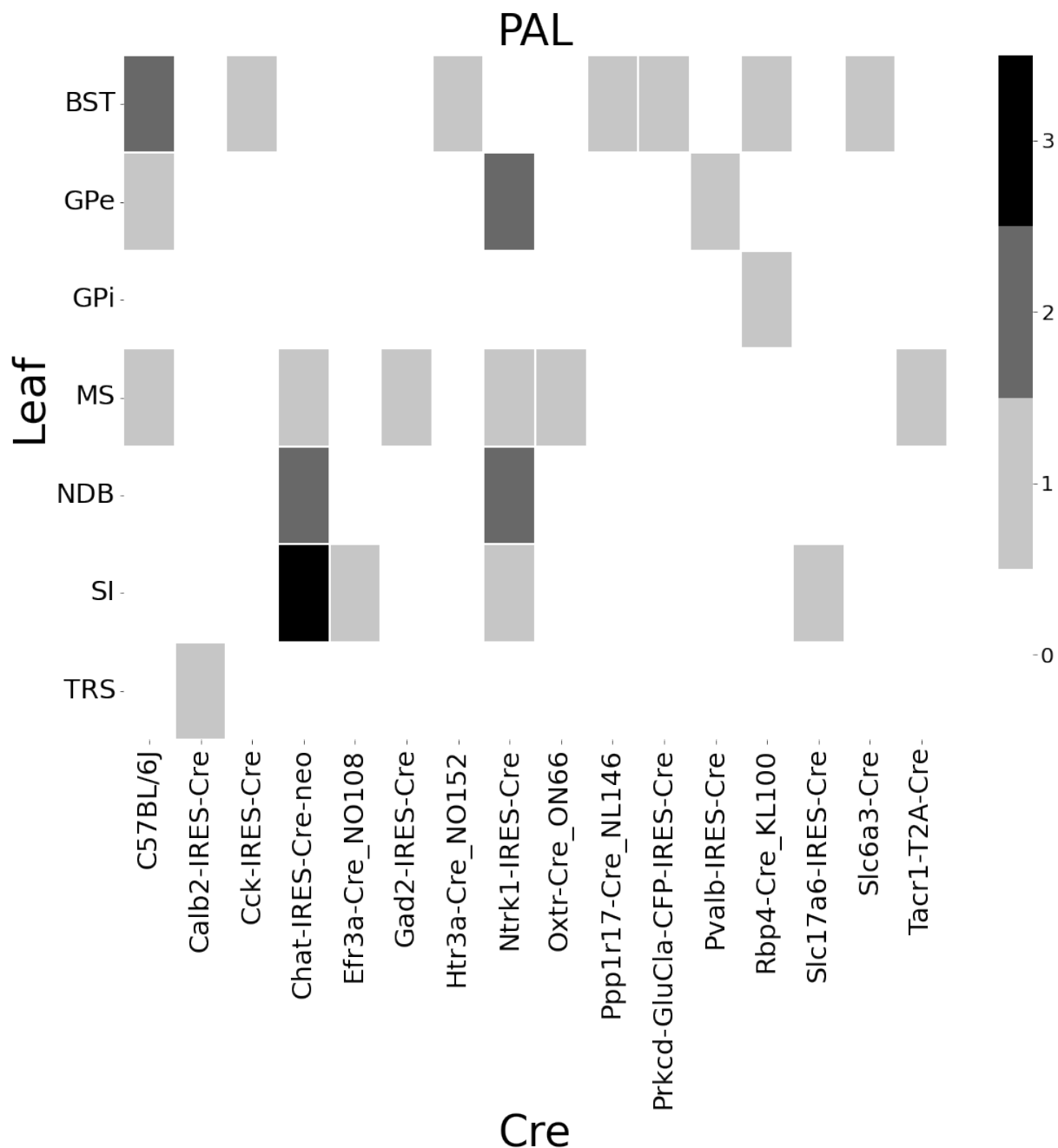


Figure 9: Abundances of Cre-line and leaf-centroid combinations.

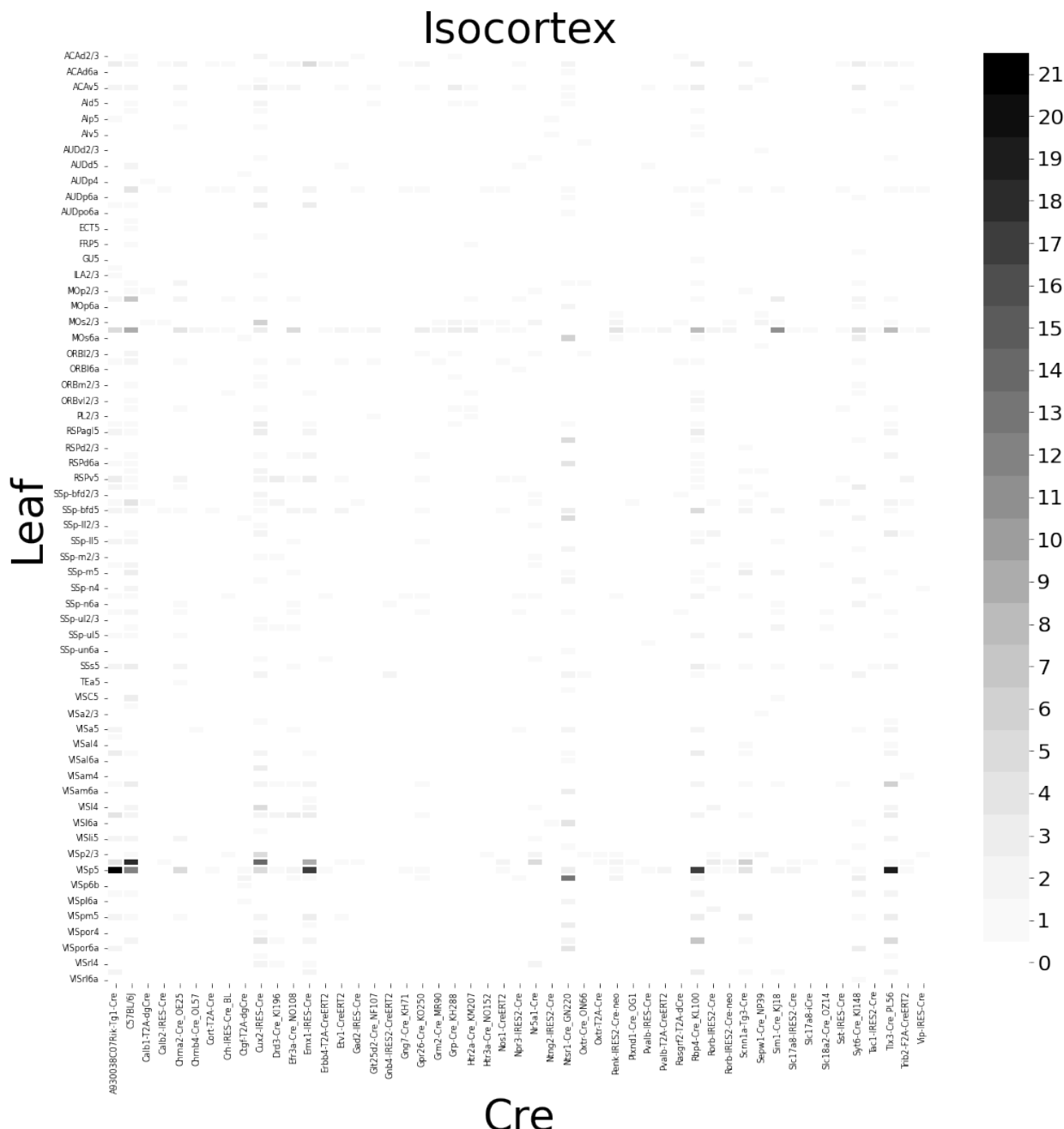


Figure 10: Abundances of Cre-line and leaf-centroid combinations.

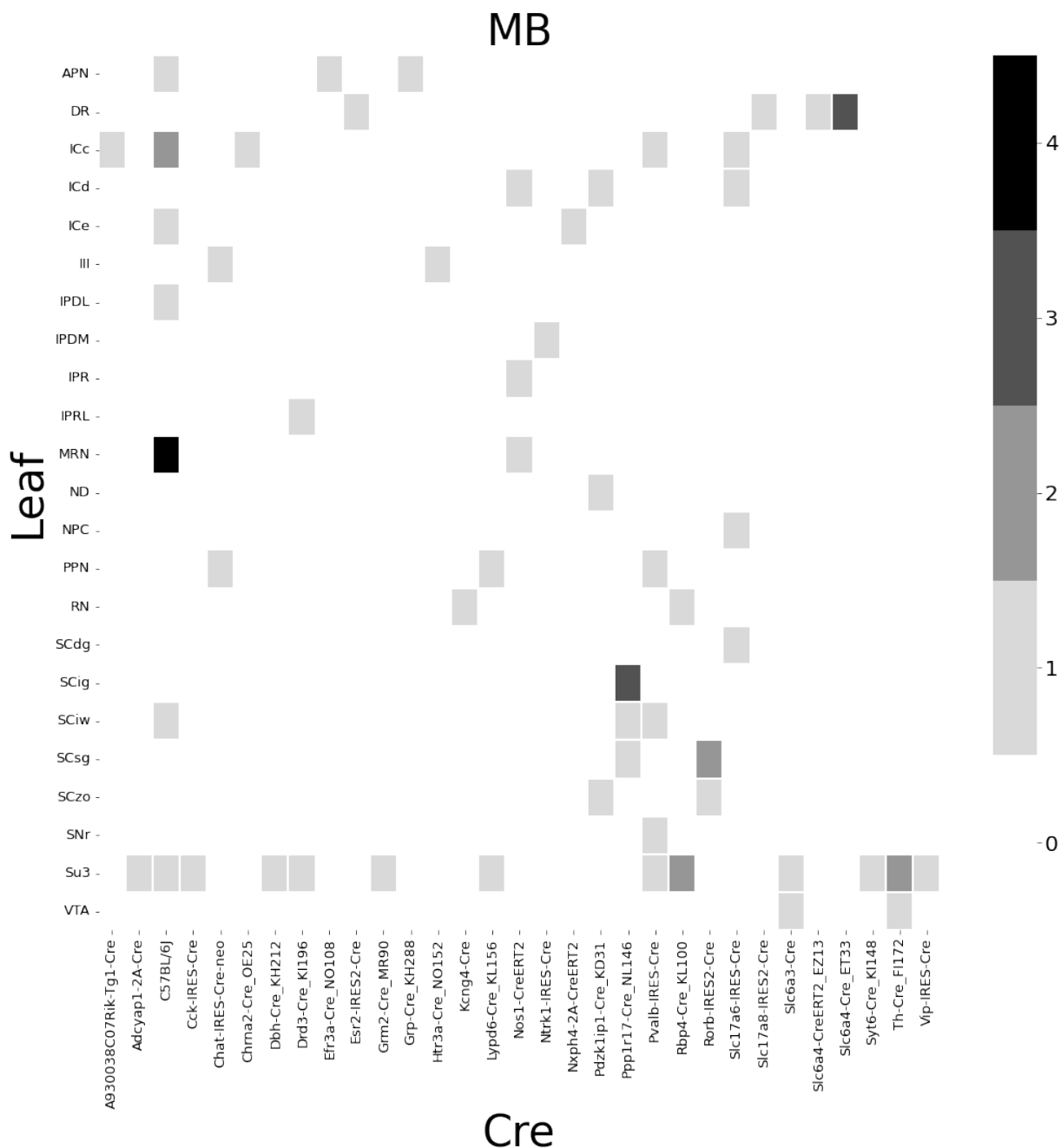


Figure 11: Abundances of Cre-line and leaf-centroid combinations.

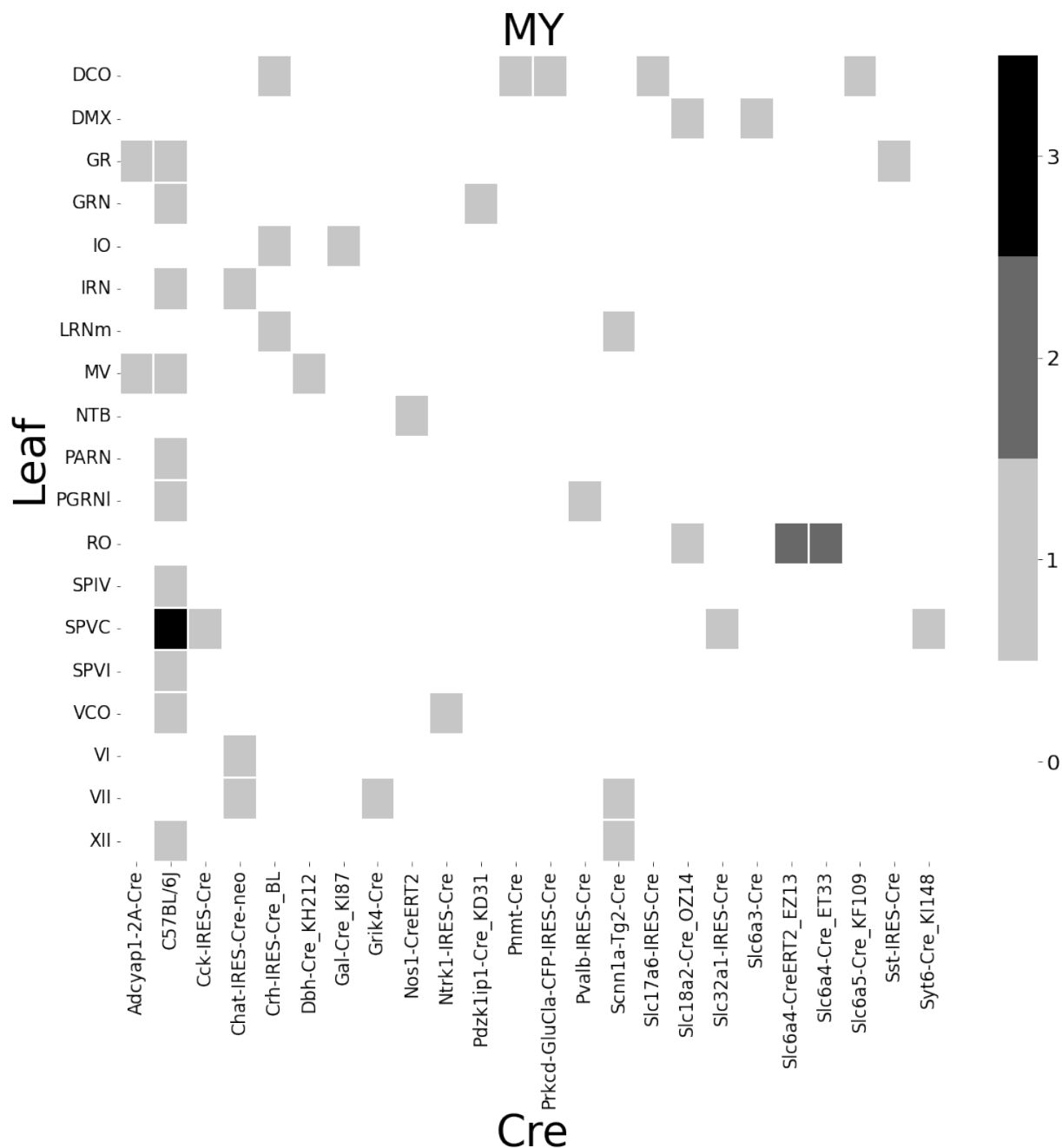


Figure 12: Abundances of Cre-line and leaf-centroid combinations.

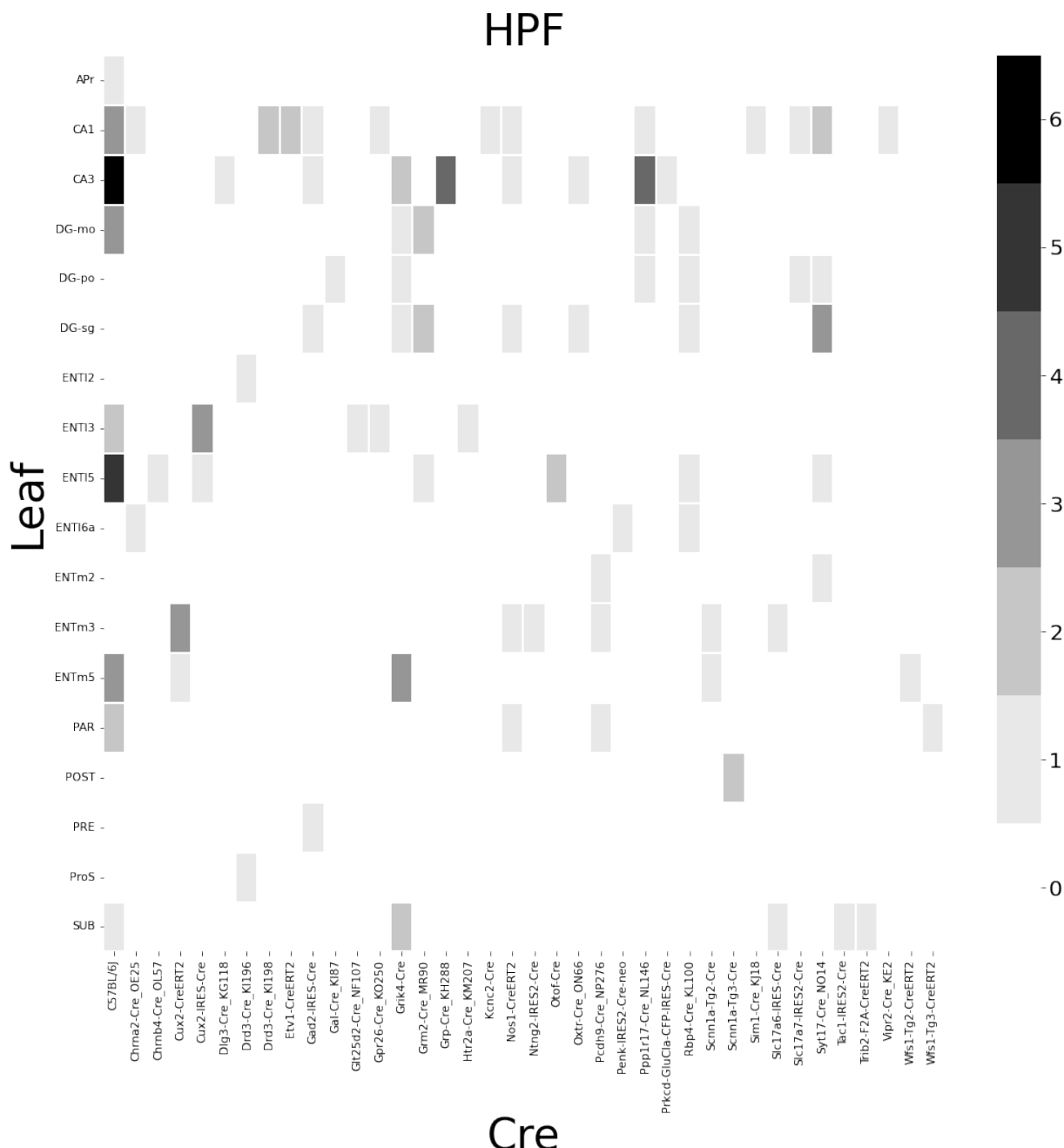


Figure 13: Abundances of Cre-line and leaf-centroid combinations.

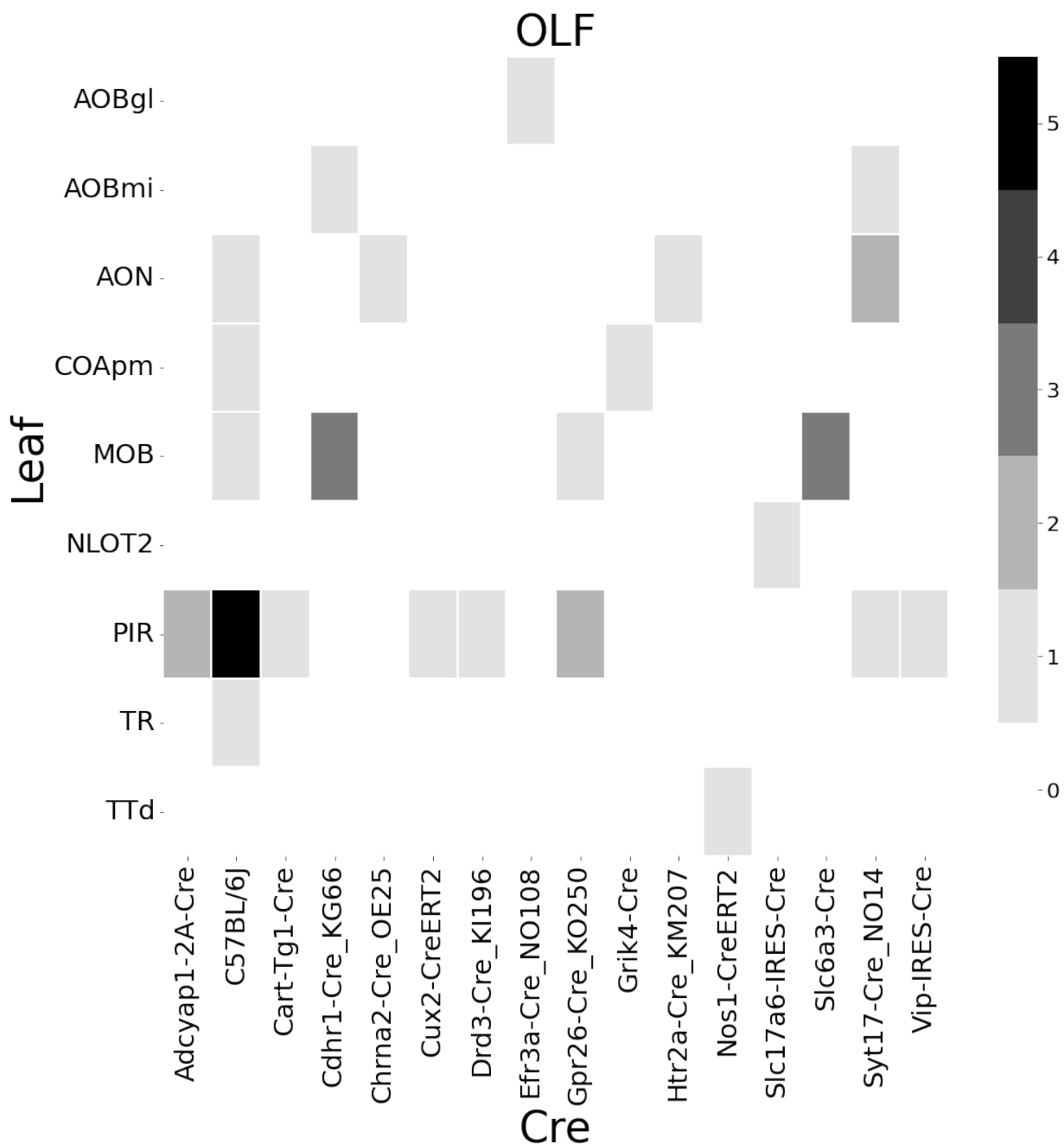


Figure 14: Abundances of Cre-line and leaf-centroid combinations.

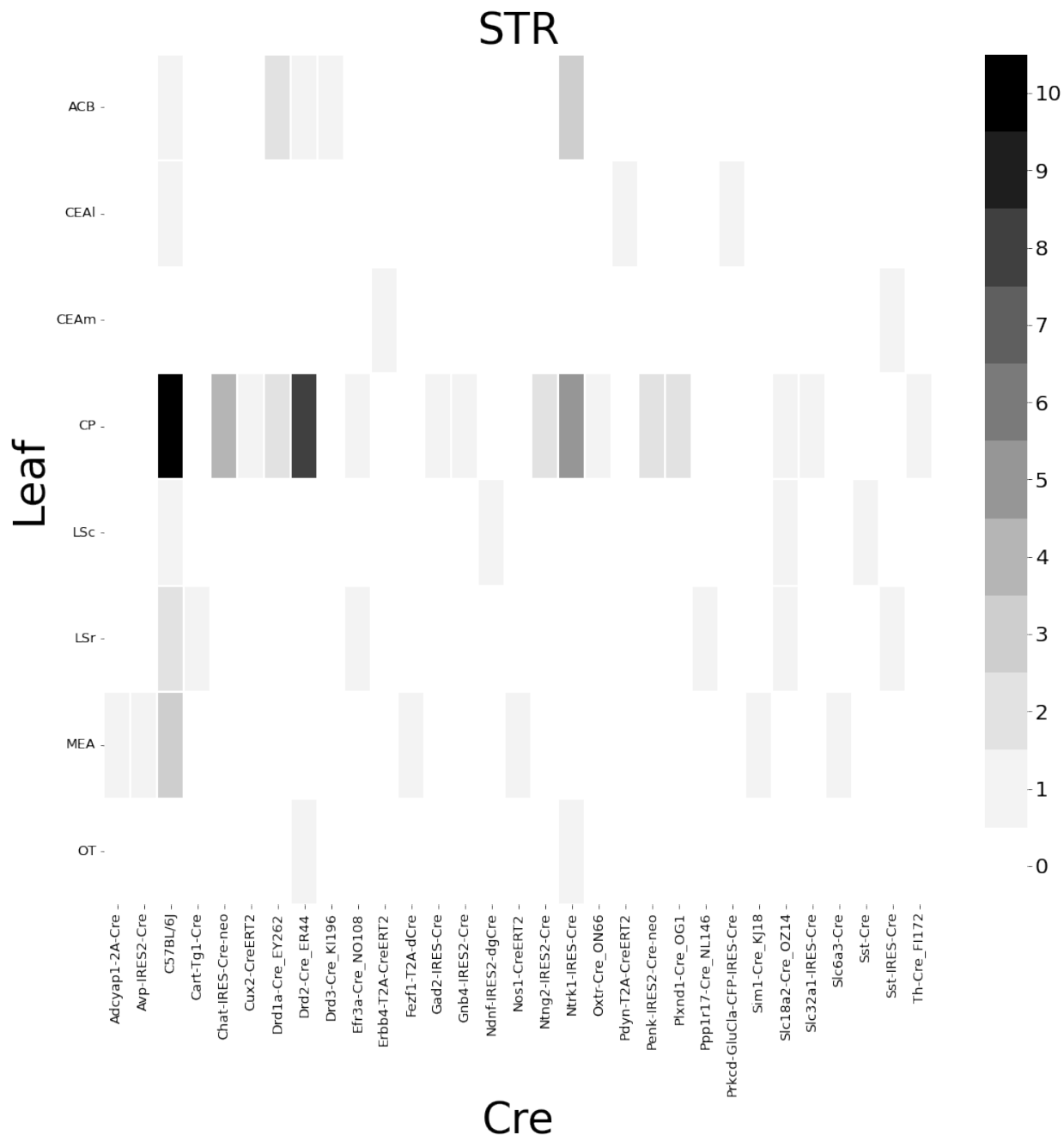


Figure 15: Abundances of Cre-line and leaf-centroid combinations.

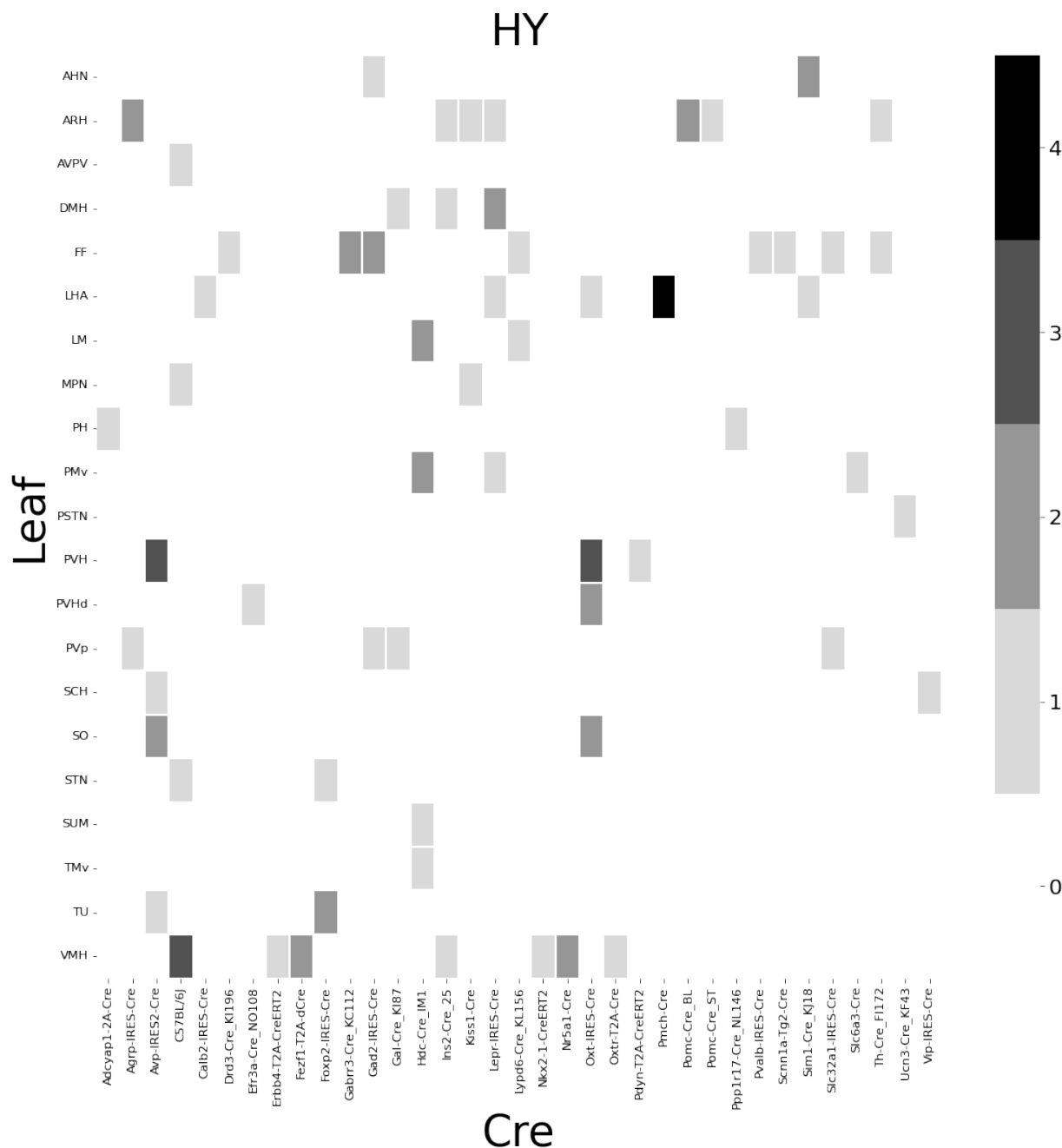


Figure 16: Abundances of Cre-line and leaf-centroid combinations.

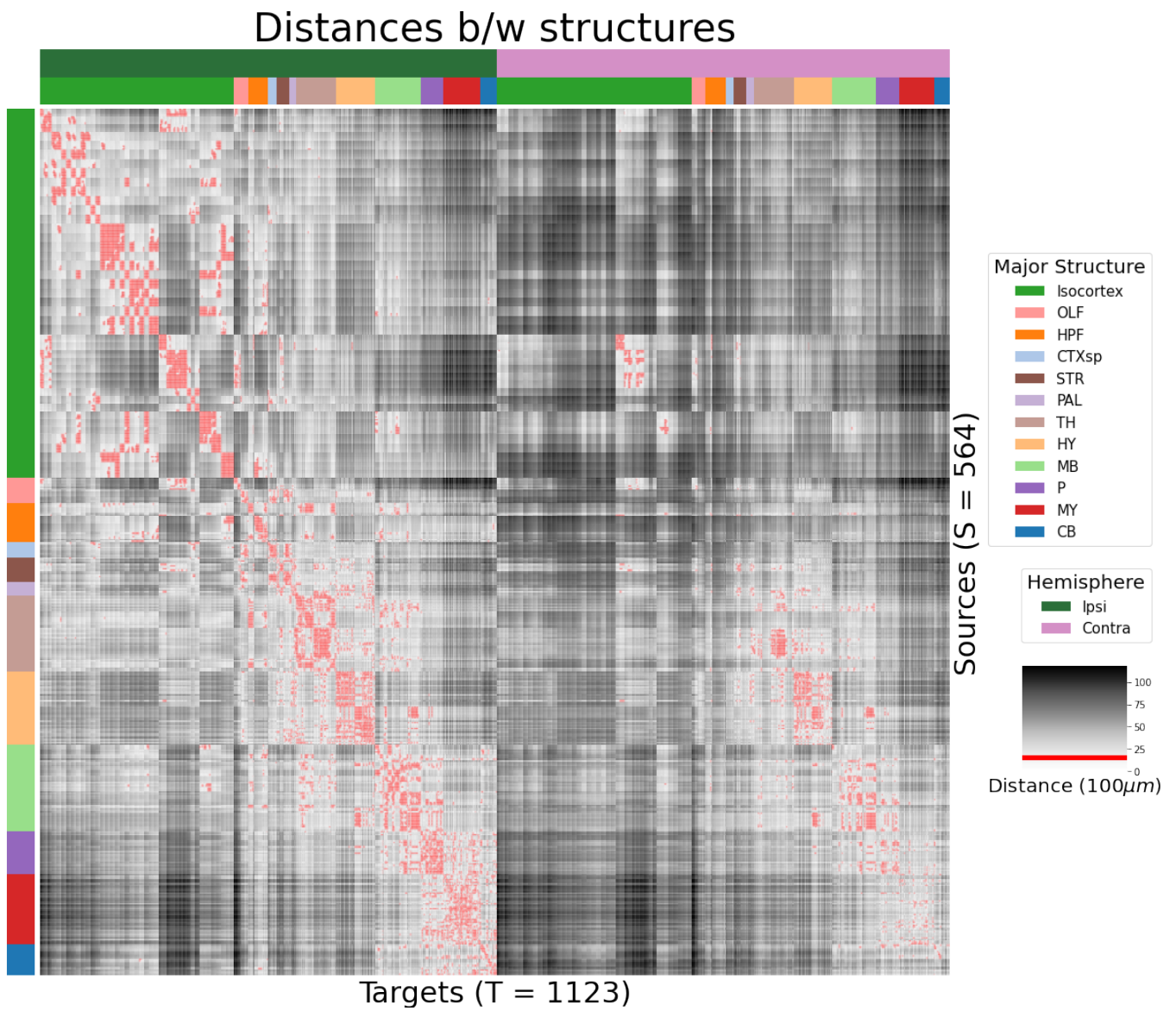
405 ***Distances between structures***

Figure 17: Distance between structures. Short-range connections are masked in red

406 ***Model evaluation***

407 We give information on the quality of our models. This includes the sizes of our evaluation sets in
 408 leave-one-out cross-validation and additional losses in the injection-normalized case.

409 NUMBER OF EXPERIMENTS IN EVALUATION SETS In order to compare between methods, we therefore
 410 restrict to the smallest set of evaluation indices, which is to say, virus-leaf combinations that are
 411 present at least twice. This means that our evaluation set is smaller in size than our overall list of
 412 experiments.

	Total	Cre-Leaf	Cre-leaf over threshold
Isocortex	36	4	4
OLF	7	2	2
HPF	122	62	59
CTXsp	85	41	38
STR	1128	732	7
PAL	68	18	17
TH	46	7	7
HY	35	17	17
MB	33	8	8
P	30	11	11
MY	78	45	44
CB	83	29	29

Table 3: Number of experiments available to evaluate models in leave-one-out cross validation. Models that rely on a finer granularity of modeling have less data available to validate with.

413 INJECTION-NORMALIZED LOSSES To compare with the injection-normalization procedure from Knox
 414 et al. (2019), we also remove experiments with small injection, and here give results for this slightly
 415 reduced set using injection-normalization. That is, instead of dividing the projection signal of each
 416 experiment by its l_1 norm, we divide by the l_1 norm of the corresponding injection signal. We find
 417 that setting a summed injection-signal of threshold of 1 is sufficient for evading pathological edge
 418 cases in this normalization, while still retaining a large evaluation set.

\hat{f}	Mean	NW	EL				
\mathcal{D}	$I_c \cap I_L$	$I_c \cap I_M$	$I_c \cap I_L$	I_L	$I_{wt} \cap I_M$	I_M	I_L
Isocortex	0.413	0.453	0.408	0.538	0.528	0.528	0.396
OLF	0.499	0.504	0.494	0.441	0.543	0.543	0.437
HPF	0.336	0.483	0.332	0.444	0.501	0.501	0.321
CTXsp	0.497	0.497	0.497	0.497	0.497	0.497	0.497
STR	0.359	0.386	0.359	0.364	0.433	0.433	0.322
PAL	0.519	0.497	0.519	0.436	0.459	0.459	0.434
TH	0.769	0.767	0.769	0.514	0.539	0.539	0.556
HY	0.414	0.439	0.414	0.441	0.452	0.452	0.399
MB	0.459	0.396	0.397	0.358	0.324	0.324	0.403
P	0.562	0.562	0.562	0.758	0.764	0.764	0.562
MY	0.699	0.552	0.621	0.439	0.578	0.578	0.439
CB	0.849	0.689	0.849	0.500	0.615	0.615	0.495

Table 4: Losses from leave-one-out cross-validation of candidate for injection-normalized regionalized connectivity on injection-thresholded evaluation set. **Bold** numbers are best for their major structure.

419 PROJECTION-NORMALIZED LOSSES ON THRESHOLDED SET We also give results for the
 420 projection-normalization procedure from the main text on this reduced subset.

\hat{f}	Mean	NW	EL				
\mathcal{D}	$I_c \cap I_L$	$I_c \cap I_M$	$I_c \cap I_L$	I_L	$I_{wt} \cap I_M$	I_M	I_L
Isocortex	0.229	0.248	0.224	0.274	0.269	0.269	0.217
OLF	0.193	0.233	0.191	0.135	0.179	0.179	0.138
HPF	0.178	0.342	0.172	0.212	0.235	0.235	0.172
CTXsp	0.621	0.621	0.621	0.621	0.621	0.621	0.621
STR	0.128	0.117	0.124	0.171	0.234	0.234	0.125
PAL	0.203	0.205	0.203	0.295	0.291	0.291	0.188
TH	0.673	0.664	0.673	0.358	0.379	0.379	0.417
HY	0.358	0.378	0.351	0.331	0.312	0.312	0.314
MB	0.168	0.191	0.160	0.199	0.202	0.202	0.160
P	0.292	0.292	0.292	0.299	0.299	0.299	0.287
MY	0.268	0.347	0.268	0.167	0.189	0.189	0.196
CB	0.062	0.062	0.062	0.068	0.108	0.108	0.061

Table 5: Losses from leave-one-out cross-validation of candidate for normalized regionalized connectivity on injection-thresholded evaluation set. **Bold** numbers are best for their major structure.

6 SUPPLEMENTAL METHODS

⁴²¹ This section consists of additional information on preprocessing of the neural connectivity data,
⁴²² estimation of connectivity, and matrix factorization.

⁴²³ ***Data preprocessing***

⁴²⁴ Several data preprocessing steps take place prior to evaluations of the connectivity matrices. These
⁴²⁵ steps are described in Algorithm PREPROCESS. The arguments of this normalization process - injection
⁴²⁶ signals $x(i)$, projection signals $y(i)$, injection fraction $F(i)$, and data quality mask $q(i)$ - were
⁴²⁷ downloaded using the Allen SDK. The injections and projection signals $\mathcal{B} \rightarrow [0, 1]$ were segmented
⁴²⁸ manually in histological analysis. The projection signal gives the proportion of pixels within the voxel
⁴²⁹ displaying fluorescence, and the injection signal gives the proportion of pixels within the
⁴³⁰ histologically-selected injection subset displaying fluorescence. The injection fraction $\mathcal{B} \rightarrow [0, 1]$ gives
⁴³¹ the proportion of pixels within each voxel in the injection subset. Finally, the data quality mask
⁴³² $\mathcal{B} \rightarrow \{0, 1\}$ gives the voxels that have valid data.

⁴³³ Our preprocessing makes use of the above ingredients, as well as several other essential steps. First,
⁴³⁴ we compute the weighted injection centroid

$$c(i) = \sum_{l \in \mathcal{B}} x(l) l$$

⁴³⁵ where $x(i)(l)$ is the injection density at location $l \in \mathbb{R}^3$. Given a regionalization \mathcal{R} from the Allen SDK,
⁴³⁶ we can also access regionalization map $R: \mathcal{B} \rightarrow \mathcal{R}$. This induces a functional of connectivities from
⁴³⁷ the space of maps $\{\mathcal{X} = x: \mathcal{B} \rightarrow [0, 1]$

$$\begin{aligned} 1_{\mathcal{R}}: \mathcal{X} &\rightarrow \mathcal{R} \times \mathbb{R}_{\geq 0} \\ x &\mapsto \sum_{l \in r} x(l) \text{ for } r \in \mathcal{R}. \end{aligned}$$

⁴³⁸ We also can restrict a signal to a individual structure as

$$\begin{aligned} 1|_s: \mathcal{X} &\rightarrow \mathcal{X} \\ x(l) &= \begin{cases} x(l) & \text{if } l \in S \\ 0 & \text{otherwise.} \end{cases} \end{aligned}$$

⁴³⁹ Finally, given a vector or array $a \in \mathbb{R}^T$, we have the $l1$ normalization map

$$n: a \mapsto \frac{a}{\sum_{j=1}^T a_j}.$$

⁴⁴⁰ We define these objects as functions and functionals, but this is for notational convenience and

⁴⁴¹ non-essential. A function $x(i) : \mathcal{B} \rightarrow [0, 1]$ is mathematically equivalent to the graph

⁴⁴² $\mathcal{G}(x(i)) \in \mathcal{B} \times [0, 1]$. As an abuse of notation, we define $x \odot x' := z$ such that $z(l) = x(l)x'(l)$ for all $l \in \mathcal{B}$.

⁴⁴³ Also, denote $m(i)$ as the major structure containing experiment i . We then can write the

⁴⁴⁴ preprocessing algorithm.

PREPROCESS 1 Input Injection x , Projection y , Injection centroid $c \in \mathbb{R}^3$, Injection fraction F , data quality mask q

Injection fraction $x_F \leftarrow x \odot F$

Data-quality censor $y_q \leftarrow y \odot q$, $x_q \leftarrow x_F \odot q$

Restrict injection $x_m = 1|_m x_q$.

Compute centroid c from x_m

Regionalize $\tilde{y}_{\mathcal{T}} \leftarrow 1_{\mathcal{T}}(y_q)$

Normalize $y_{\mathcal{T}} \leftarrow n(\tilde{y}_{\mathcal{T}})$

Output $\tilde{y}_{\mathcal{T}}, c$

445 Estimators

446 As mentioned previously, we can consider our estimators as modeling a connectivity vector
 447 $f_{\mathcal{T}}(\nu, s) \in \mathbb{R}_{\geq 0}^T$. Thus, for the remainder of this section, we will discuss only $f(\nu, s)$. We review the
 448 Nadaraya-Watson estimator from Knox et al. (2019), and describe its conversion into our cell-class
 449 specific Expected Loss estimator.

450 *Centroid-based Nadaraya-Watson* In the Nadaraya-Watson approach of Knox et al. (2019), the injection
 451 is considered only through its centroid $c(i)$, and the projection is considered regionalized. That is,

$$f_*(i) = \{c(i), y_{\mathcal{T}}(i)\}.$$

452 Since the injection is considered only by its centroid, this model only generates predictions for
 453 particular locations l , and the prediction for a structure s is given by integrating over locations within
 454 the structure

$$f^*(\hat{f}(f_*(\mathcal{D})))(\nu, s) = \sum_{l \in s} \hat{f}(f_*(\mathcal{D}(I)))(\nu, l).$$

455 Here, I is the training data, and \hat{f} is the Nadaraya-Watson estimator

$$\hat{f}_{NW}(c(I), y_{\mathcal{T}}(I))(l) := \sum_{i \in I} \frac{\omega_{il}}{\sum_{i \in I} \omega_{il}} y_{\mathcal{T}}(i)$$

456 where $\omega_{il} := \exp(-\gamma d(l, c(i))^2)$ and d is the Euclidean distance between centroid $c(i)$ and voxel with
 457 position l .

458 Several facets of the estimator are visible here. A smaller γ corresponds to a greater amount of
 459 smoothing, and the index set $I \subseteq \{1 : n\}$ generally depends on s and ν . Varying γ bridges between
 460 1-nearest neighbor prediction and averaging of all experiments in I . In Knox et al. (2019), I consisted
 461 of experiments sharing the same brain division, i.e. $I = I_m$, while restricting of index set to only
 462 include experiments with the same cell class gives the class-specific Cre-NW model. Despite this
 463 restriction, we fit γ by leave-one-out cross-validation for each m rather than a smaller subset like s or
 464 ν . That is,

$$\hat{\gamma}_m = \arg \min_{\gamma \in \mathbb{R}_{\geq 0}} \frac{1}{|\{s, \nu\}|} \sum_{s, \nu \in \{m, \mathcal{V}\}} \frac{1}{|I_s \cap I_\nu|} \sum_{i \in (I_s \cap I_\nu)} \ell(y_{\mathcal{T}}(i)), \hat{f}_{\mathcal{T}}(f_*(\mathcal{D}(\nu, s) \setminus i)). \quad (2)$$

⁴⁶⁵ *The Expected-Loss estimator* Besides location of the injection centroid, cell class also influences
⁴⁶⁶ projection. Thus, we introduce method for estimating the effect of Cre-distance, which we define as
⁴⁶⁷ the distance between the projections of the mean experiment of one (Cre,leaf) pair with another. This
⁴⁶⁸ method assigns a predictive weight to each pair of training points that depends both on their
⁴⁶⁹ centroid-distance and Cre-distance. This weight is determined by the expected prediction error of
⁴⁷⁰ each of the two feature types

⁴⁷¹ We define Cre-line behavior as the average regionalized projection of a Cre-line in a given structure
⁴⁷² (i.e. leaf). The vectorization of categorical information is known as **target encoding**

$$\bar{y}_{\mathcal{T},s,v} := \frac{1}{|I_s \cap I_v|} \sum_{i \in (I_s \cap I_v)} y_{\mathcal{T}}(i)$$

⁴⁷³ The Cre-distance is then defined a **Cre-distance** in a leaf to be the distance between the target-encoded
⁴⁷⁴ projections of two Cre-lines. The relative predictive accuracy of Cre-distance and centroid distance is
⁴⁷⁵ determined by fitting a surface of projection distance as a function of Cre-distance and centroid
⁴⁷⁶ distance.

⁴⁷⁷ as determined by cross-validation. When we use shape-constrained B-splines to estimate this
⁴⁷⁸ weight, the weights then may be said to be used in a Nadaraya-Watson estimator.

⁴⁷⁹ For this reason, we call this the Expected Loss Estimator. The resulting weights are then utilized in a
⁴⁸⁰ Nadaraya-Watson estimator in a final prediction step. increase the effective sample size of our
⁴⁸¹ Nadaraya-Watson estimator,

⁴⁸² In mathematical terms, our full feature set consists of the centroid coordinates and the
⁴⁸³ target-encoded means of the combinations of virus type and injection-centroid structure. That is,

$$f_*(\mathcal{D}_i) = \{c(i), \{\bar{y}_{\mathcal{T},s,v} \forall v\}, y_{\mathcal{T}}(i)\}.$$

⁴⁸⁴ f^* is defined as in (2). The expected loss estimator is then

$$\hat{f}_{EL}(c(I), y_{\mathcal{T}}(I))(l, v) := \sum_{i \in I} \frac{v_{ilv}}{\sum_{i \in I} v_{ilv}} y_{\mathcal{T}}(i)$$

⁴⁸⁵ where

$$v_{ilv} := \exp(-\gamma g(d(l, c(i))^2, d(\bar{y}_{\mathcal{T},s,v}, \bar{y}_{\mathcal{T},s,v(i)})^2))$$

⁴⁸⁶ and s is the structure containing l .

⁴⁸⁷ The key step therefore is finding a suitable function g with which to weight the positional and Cre
⁴⁸⁸ information. Note that g must be a concave, non-decreasing function of its arguments with with
⁴⁸⁹ $g(0, 0) = 0$. Then, g defines a metric on the product of the metric spaces defined by experiment
⁴⁹⁰ centroid and target-encoded cre-line, and \hat{f}_{EL} is a Nadaraya-Watson estimator. A derivation of this
⁴⁹¹ fact is given later in this section.

⁴⁹² therefore use shape-constrained B-splines to estimate g . In particular, B-splines is a method for
⁴⁹³ generating a predictive model

$$y =$$

⁴⁹⁴ In our setting, this gives us a surface the Cre-distance and centroid-distance to the
⁴⁹⁵ projection-distance response. Similarly to the Nadaraya-Watson model, we make the decision to fit a
⁴⁹⁶ g separately for each major brain division, and select \hat{g} as in 2. We compute our estimates using the
⁴⁹⁷ pyGAM Python package (Servén D., n.d.).

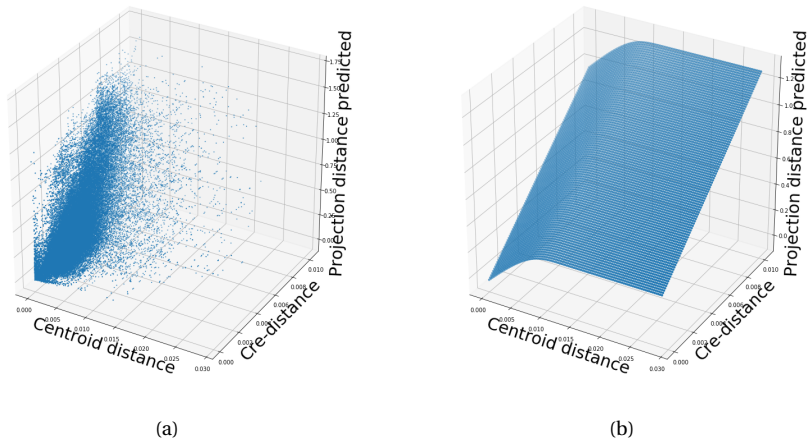


Figure 18: Fitting g . 18a Distribution of projection errors against centroid distance and cre-distance in Isocortex. 18b estimated \hat{g} using B-splines.

498 JUSTIFICATION OF SHAPE CONSTRAINT The shape-constrained expected-loss estimator introduced
 499 in this paper is, to our knowledge, novel. It should be considered an alternative method to the classic
 500 weighted kernel method. While we do not attempt a detailed theoretical study of this estimator, we do
 501 establish the need for the shape constraint in our spline estimator. Though this fact is probably well
 502 known, we prove a (slightly stronger) version here for completeness.

503 **Proposition 1.** *Given a collection of metric spaces X_1, \dots, X_n with metrics d_1, \dots, d_n (e.g. $d_{centroid}, d_{cre}$),
 504 and a function $f : (X_1 \times X_1) \dots \times (X_n \times X_n) = g(d_1(X_1 \times X_1), \dots, d_n(X_n \times X_n))$, then f is a metric if g is
 505 concave, non-decreasing and $g(d) = 0 \iff d = 0$.*

506 *Proof.* We show g satisfying the above properties implies that f is a metric.

- 507 ▪ The first property of a metric is that $f(x, x') = 0 \iff x = x'$. The left implication:
 508 $x = x' \implies f(x_1, x'_1, \dots, x_n, x'_n) = g(0, \dots, 0)$, since d are metrics. Then, since $g(0) = 0$, we have that
 509 $f(x, x') = 0$. The right implication: $f(x, x') = 0 \implies d = 0 \implies x = x'$ since d are metrics.
- 510 ▪ The second property of a metric is that $f(x, x') = f(x', x)$. This follows immediately from the
 511 symmetry of the d_i , i.e. $f(x, x') = f(x_1, x'_1, \dots, x_n, x'_n) = g(d_1(x_1, x'_1), \dots, d_n(x_n, x'_n)) =$
 512 $g(d_1(x'_1, x_1), \dots, d_n(x'_n, x_n)) = f(x'_1, x_1, \dots, x'_n, x_n) = f(x', x)$.
- 513 ▪ The third property of a metric is the triangle inequality: $f(x, x') \leq f(x, x^*) + f(x^*, x')$. To show this
 514 is satisfied for such a g , we first note that $f(x, x') = g(d(x, x')) \leq g(d(x, x^*) + d(x^*, x'))$ since g is
 515 non-decreasing and by the triangle inequality of d . Then, since g is concave,
 516 $g(d(x, x^*) + d(x^*, x')) \leq g(d(x, x^*)) + g(d(x^*, x')) = f(x, x^*) + f(x^*, x')$.

518 ***Setting a lower detection threshold***

519 The lower detection threshold of our approach is a complicated consequence of our experimental and
 520 analytical protocols. For example, the Nadaraya-Watson estimator is likely to generate many small
 521 false positive connections, since the projection of even a single experiment within the source region
 522 to a target will cause a non-zero connectivity in the Nadaraya-Watson weighted average. On the other
 523 hand, the complexities of the experimental protocol itself and the image analysis and alignment can
 524 also cause spurious signals. Therefore, it is of interest to establish a lower-detection threshold below
 525 which we have very little power-to-predict, and set estimated connectivities below this threshold to
 526 zero. This should make our estimated connectivities more accurate, especially in the
 527 biologically-important sense of sparsity.

528 We set this threshold with respect to the sum of Type 1 and Type 2 errors

$$\iota = \sum_{i \in \mathcal{E}} 1_{y_{\mathcal{T}}(i)=0}^T 1_{\hat{f}_{\mathcal{T}}(v(i), c(i)) > \tau} + 1_{y_{\mathcal{T}}(i) > 0}^T 1_{\hat{f}_{\mathcal{T}}(v(i), c(i)) < \tau}.$$

529 We then select the τ that minimizes ι . Results for this approach are given in Supplemental Section 7.

530 ***Decomposing the connectivity matrix***

531 We utilize non-negative matrix factorization (NMF) to analyze the principal signals in our
 532 connectivity matrix. Here, we review this approach as applied to decomposition of the distal elements
 533 of the estimated connectivity matrix $\hat{\mathcal{C}}$ to identify q connectivity archetypes. Aside from the NMF
 534 program itself, the key elements are selection of the number of archetypes q and stabilization of the
 535 tendency of NMF to give random results over different initializations.

536 *Non-negative matrix factorization* As discussed in Knox et al. (2019), one of the most basic processes
 537 underlying the observed connectivity is the tendency of each source region to predominantly project
 538 to proximal regions. For example, the heatmap in Supplemental Figure 17 shows that the pattern of
 539 infrastructure distances resembles the connectivity matrix in 2. These connections are biologically
 540 meaningful, but also unsurprising, and their relative strength biases learned latent coordinate
 541 representations away from long-range structures. For this reason, we establish a $1500\mu\text{m}$ 'distal'
 542 threshold within which to exclude connections for our analysis.

543 Given a matrix $X \in \mathbb{R}_{\geq 0}^{a \times b}$ and a desired latent space dimension q , the non-negative matrix
 544 factorization is thus

$$\text{NMF}(\mathcal{C}, \lambda, q, \mathbf{1}_M) = \arg \min_{W \in \mathbb{R}_{\geq 0}^{S \times q}, H \in \mathbb{R}_{\geq 0}^{q \times T}} \frac{1}{2} \|\mathbf{1}_M \odot \mathcal{C} - WH\|_2^2 + \lambda(\|H\|_1 + \|W\|_1).$$

545 The mask $\mathbf{1}_M$ specifies this objective for detecting patterns in long-range connections. We note the
 546 existence of NMF with alternative norms for certain marginal distributions, but leave utilization of
 547 this approach for future work (Brunet, Tamayo, Golub, & Mesirov, 2004).

548 The mask $\mathbf{1}_M \in \{0, 1\}^{S \times T}$ serves two purposes. First, it enables computation of the NMF objective
 549 while excluding self and nearby connections. These connections are both strong and linearly
 550 independent, and so would unduly influence the *NMF* reconstruction error over more biologically
 551 interesting or cell-type dependent long-range connections. Second, it enables cross-validation based
 552 selection of the number of retained components.

553 *Cross-validating NMF* We review cross-validation for NMF following (?). In summary, a NMF model is
 554 first fit on a reduced data set, and an evaluation set is held out. After random masking of the
 555 evaluation set, the loss of the learned model is then evaluated on the basis of successful
 556 reconstruction of the held-out values. This procedure is performed repeatedly, with replicates of
 557 random masks at each tested dimensionality q . This determines the point past which additional
 558 hidden units provide no additional value for reconstructing the original signal.

559 The differentiating feature of cross-validation for NMF compared with supervised learning is the
 560 randomness of the masking matrix 1_M . Cross-validation for supervised learning generally leaves out
 561 entire observations, but this is insufficient for our situation. This is because, given W , our H is the
 562 solution of a regularized non-negative least squares optimization problem

$$H := \hat{e}_W(1_M \odot \mathcal{C}) = \arg \min_{\beta \in \mathbb{R}_{\geq 0}^{q \times T}} \|1_M \odot \mathcal{C} - W\beta\|_2^2 + \|\beta\|_1. \quad (3)$$

563 The negative effects of an overfit model can therefore be optimized away from on the evaluation set.

A standard solution is to generate uniformly random masks $1_{M(p)} \in \mathbb{R}^{S \times T}$ where

$$1_{M(p)}(s, t) \sim \text{Bernoulli}(p).$$

NMF is then performed using the mask $1_{M(p)}$ to get W . The cross-validation error is then

$$\epsilon_q = \frac{1}{R} \sum_{r=1}^R (\|1_{M(p)_r^c} \odot X - W(\hat{e}_W(1_{M(p)_r^c} \odot X))\|_2^2$$

where $1_{M(p)_r}^c$ is the binary complement of $1_{M(p)_r}$ and R is a number of replicates. Theoretically, the optimum number of components is then

$$\hat{q} = \operatorname{arg\,min}_q \epsilon_q.$$

564 *Stabilizing NMF* The NMF program is non-convex, and, empirically, individual replicates will not
 565 converge to the same optima. One solution therefore is to run multiple replicates of the NMF
 566 algorithm and cluster the resulting vectors. This approach raises the questions of how many clusters
 567 to use, and how to deal with stochasticity in the clustering algorithm itself. We address this issue
 568 through the notion of clustering stability (von Luxburg, 2010a).

The clustering stability approach is to generate L replicas of k-cluster partitions $\{C_{kl} : l \in 1 \dots L\}$ and then compute the average dissimilarity between clusterings

$$\xi_k = \frac{2}{L(L-1)} \sum_{l=1}^L \sum_{l'=1}^l d(C_{kl}, C_{kl'}).$$

Then, the optimum number of clusters is

$$\hat{k} = \arg \min_k \xi_k.$$

569 A review of this approach is found in von Luxburg (2010b). Intuitively, archetype vectors that cluster
 570 together frequently over clustering replicates indicate the presence of a stable clustering. For d , we
 571 utilize the adjusted Rand Index - a simple dissimilarity measure between clusterings. Note that we
 572 expect to select slightly more than the q components suggested by cross-validation, since archetype
 573 vectors which appear in one NMF replicate generally should appear in others. We then select the q
 574 clusters with the most archetype vectors - the most stable NMF results - and take the median of each
 575 cluster to create a sparse representative archetype Kotliar et al. (2019); Wu et al. (2016). We then find
 576 the according H using Program 3. Experimental results for these cross-validation and stability
 577 selection approaches are given in Supplemental Section 7.

7 SUPPLEMENTAL EXPERIMENTS

578 *Setting detection threshold τ*

579 We give results on the false detection rate at different limits of detection. These conclusively show that
 580 10^{-6} is the good threshold for our normalized data.

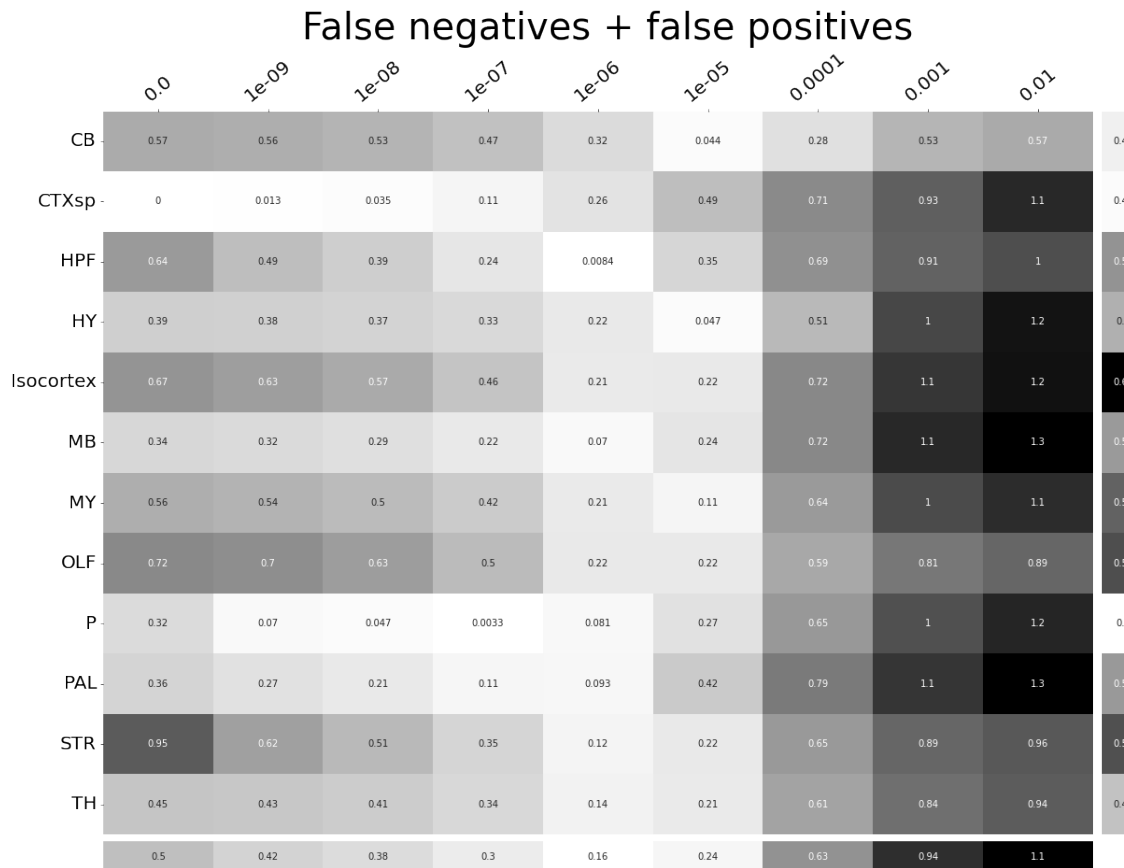


Figure 19: τ at different limits of detection in different major structures. 10^{-6} is the optimal detection threshold.

581 ***Loss subsets***

582 We report model accuracies for our *EL* model by neuron class and structure. These expand upon the
 583 results in Table 5 and give more specific information about the quality of our estimates. CTXsp is
 584 omitted due to the small nature of the evaluation set.

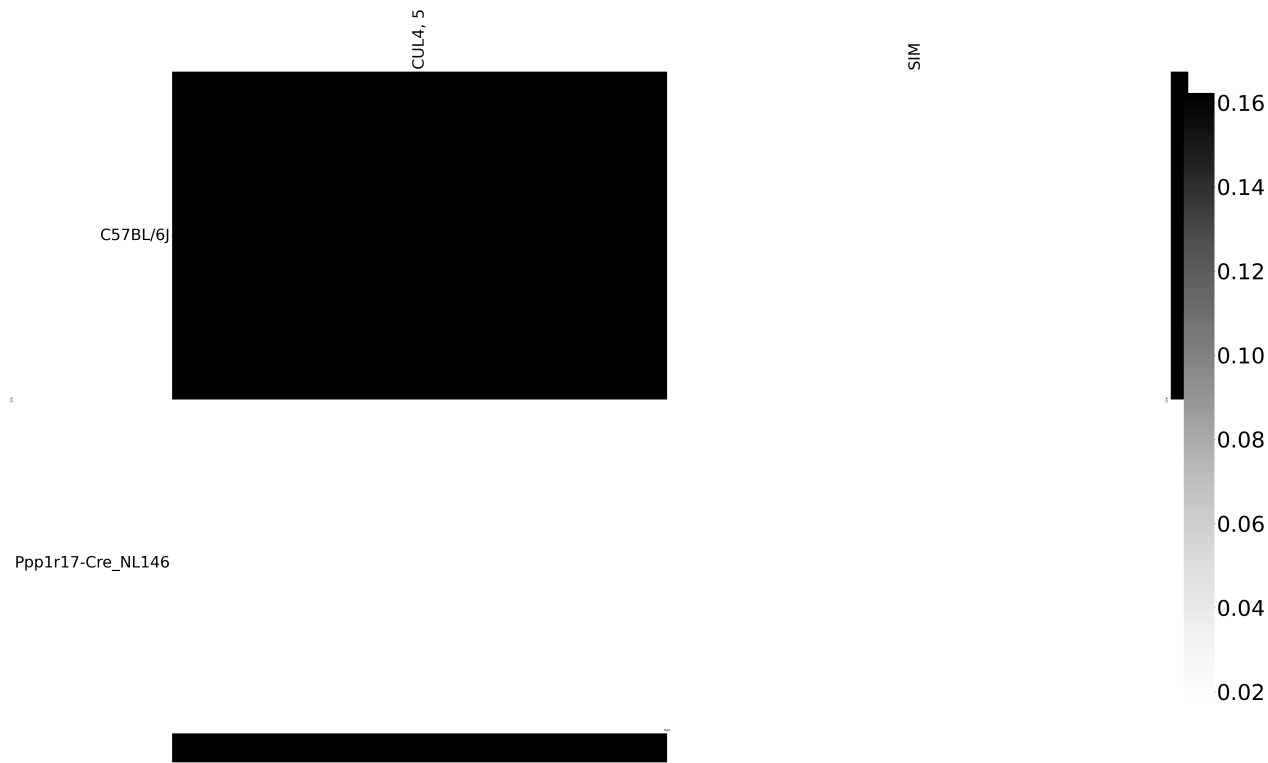


Figure 20: Weighted loss for cre-leaf combinations in CB. Missing values are omitted. Row and column averages are also plotted.

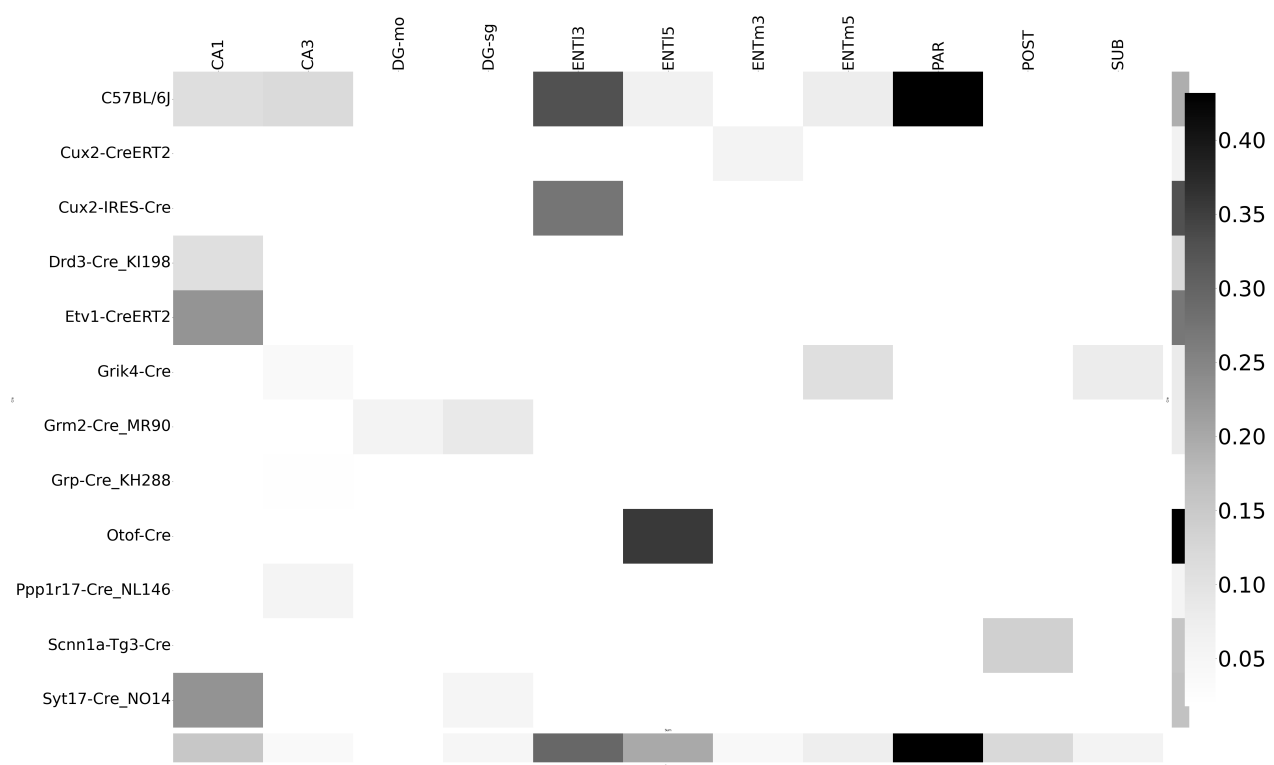


Figure 21: Weighted loss for cre-leaf combinations in HPF. Missing values are omitted. Row and column averages are also plotted.

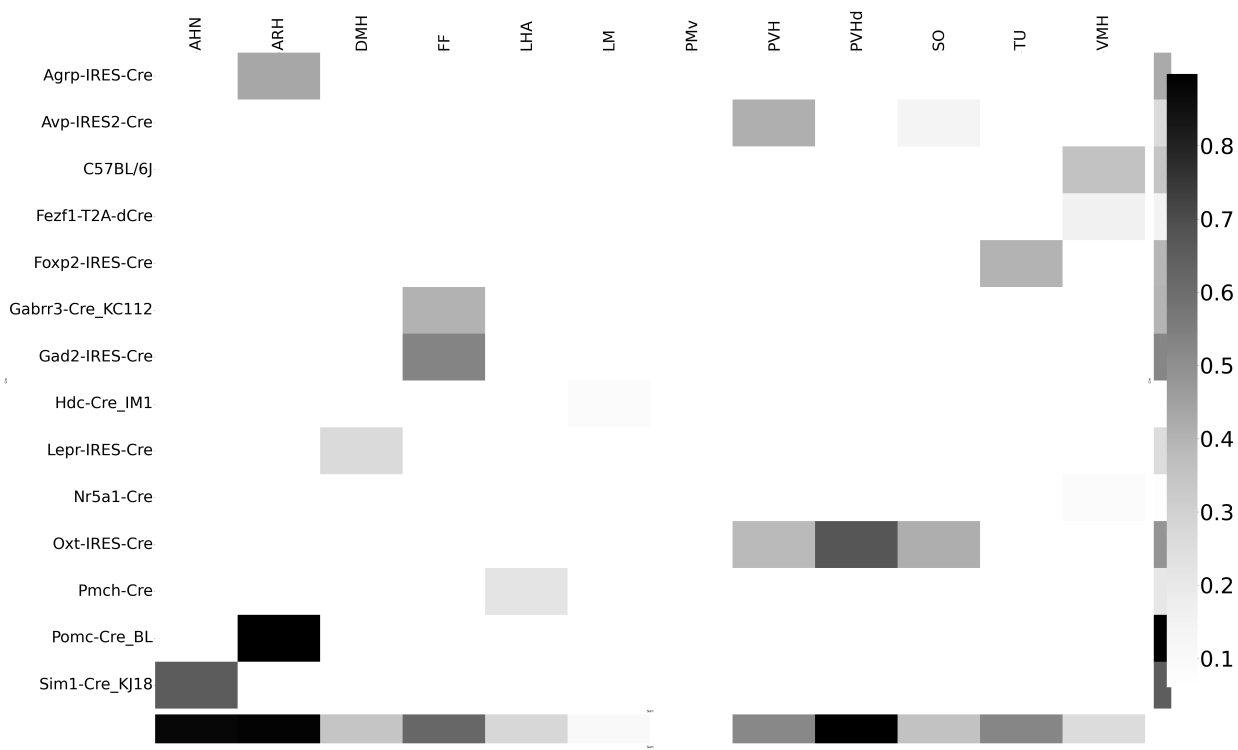


Figure 22: Weighted loss for cre-leaf combinations in HY. Missing values are omitted. Row and column averages are also plotted.

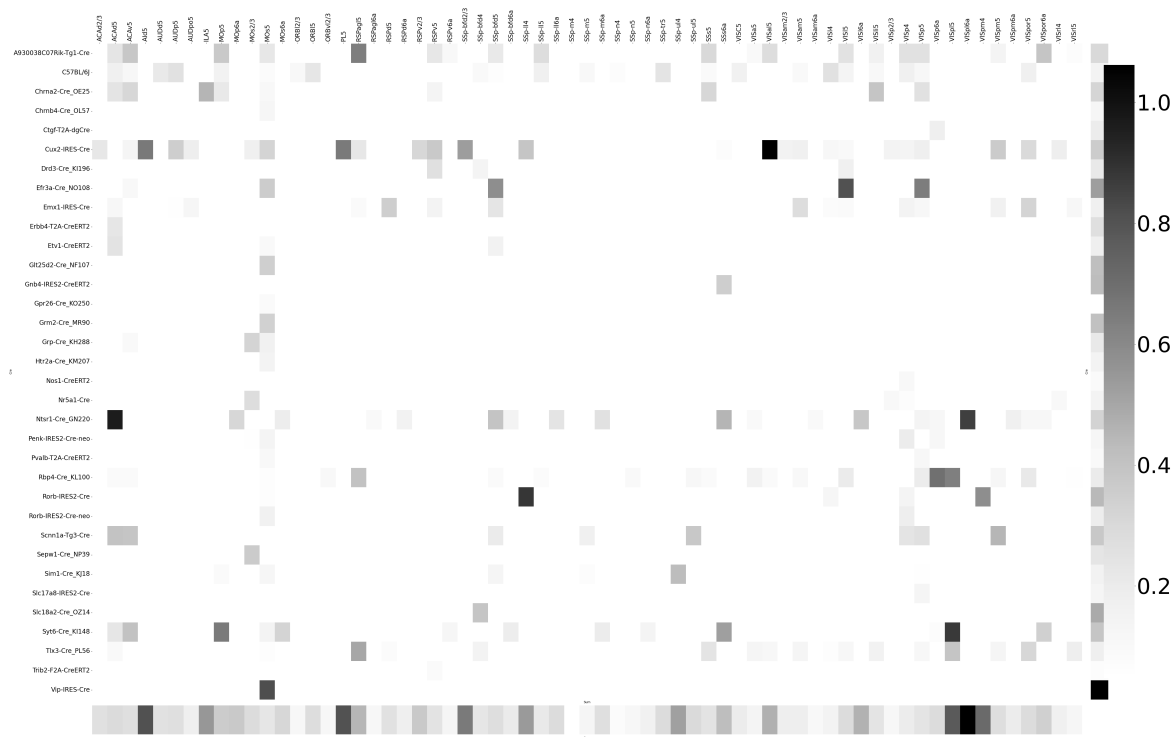


Figure 23: Weighted loss for cre-leaf combinations in Isocortex. Missing values are omitted. Row and column averages are also plotted.

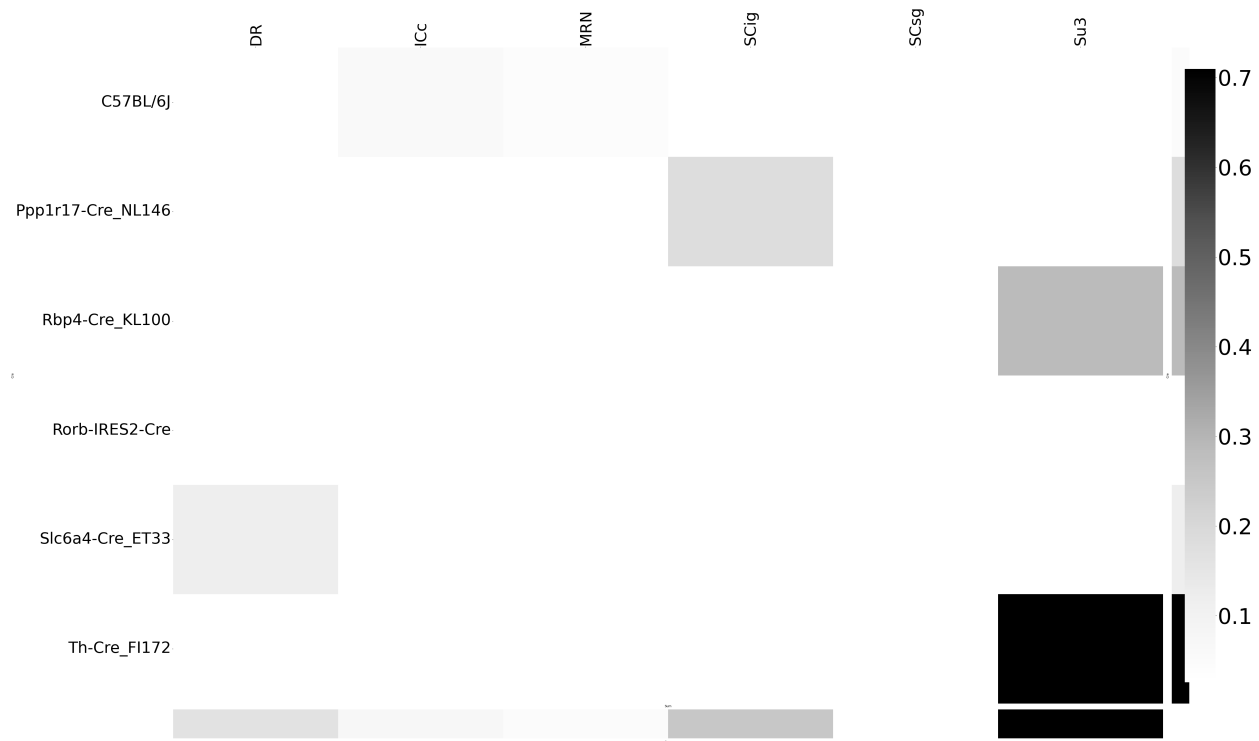


Figure 24: Weighted loss for cre-leaf combinations in MB. Missing values are omitted. Row and column averages are also plotted.

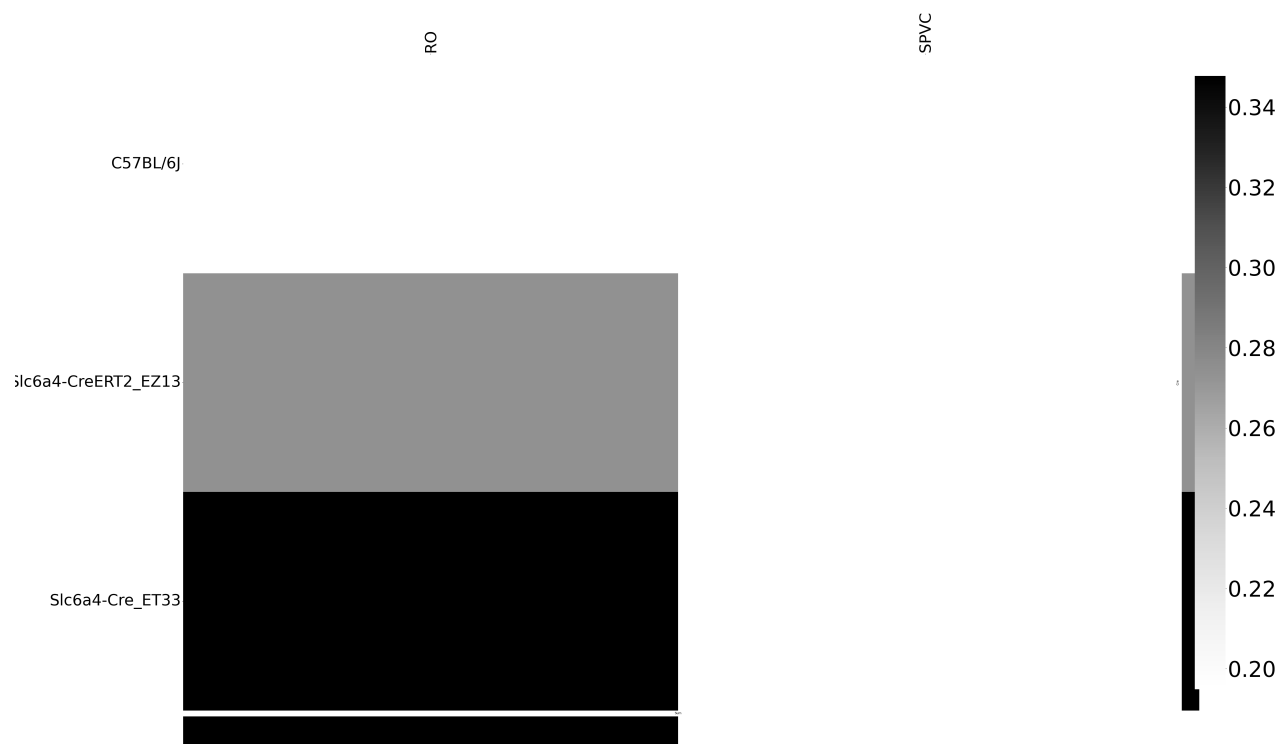


Figure 25: Weighted loss for cre-leaf combinations in MY. Missing values are omitted. Row and column averages are also plotted.

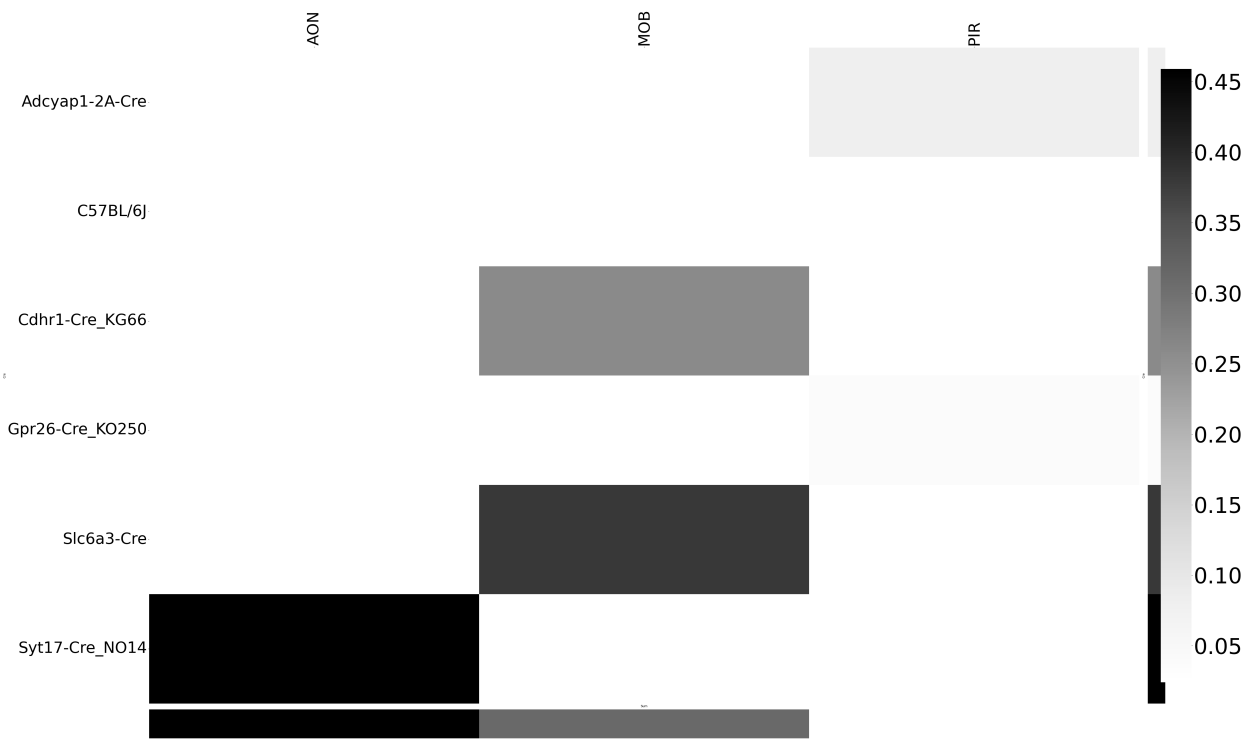


Figure 26: Weighted loss for cre-leaf combinations in OLF. Missing values are omitted. Row and column averages are also plotted.

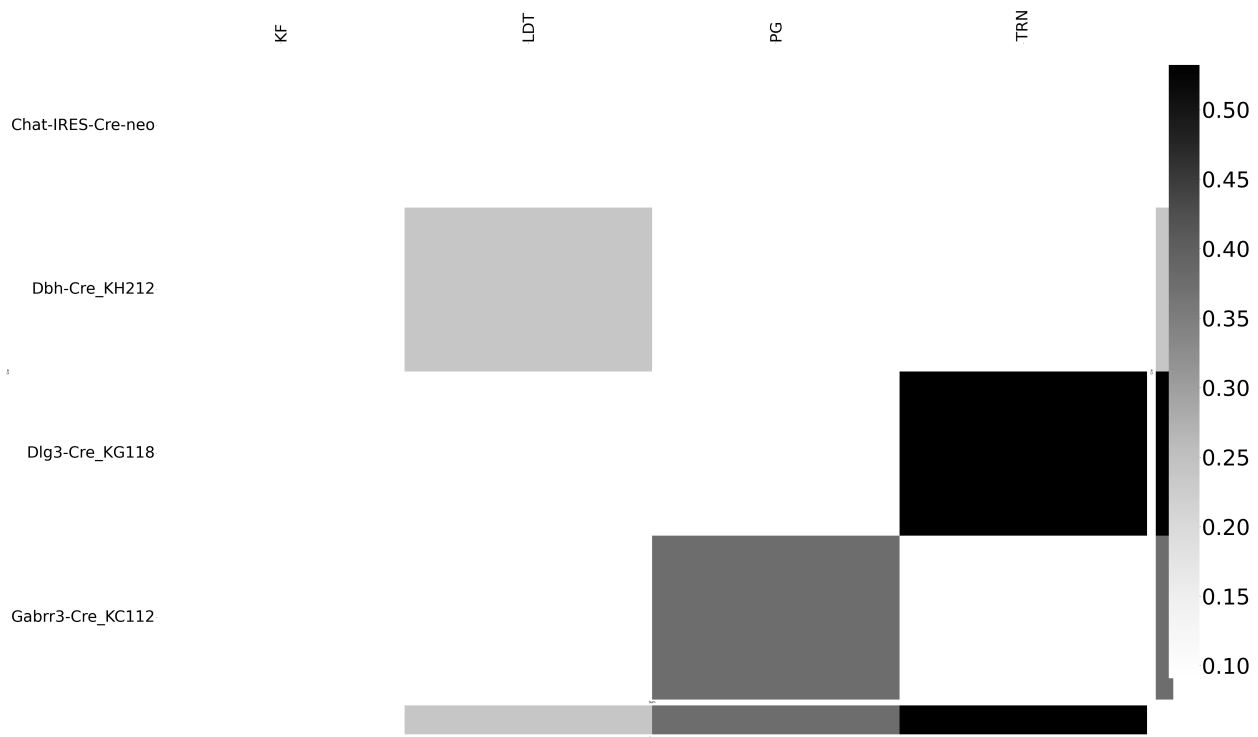


Figure 27: Weighted loss for cre-leaf combinations in P. Missing values are omitted. Row and column averages are also plotted.

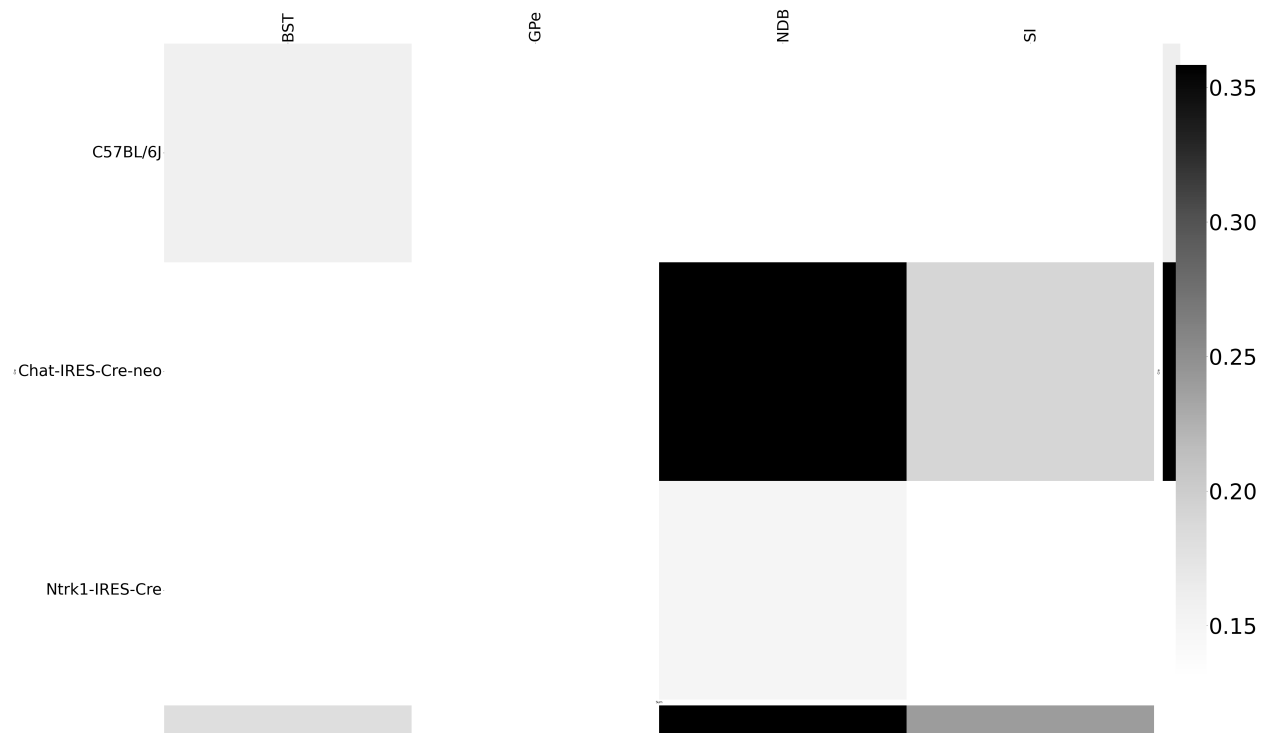


Figure 28: Weighted loss for cre-leaf combinations in PAL. Missing values are omitted. Row and column averages are also plotted.

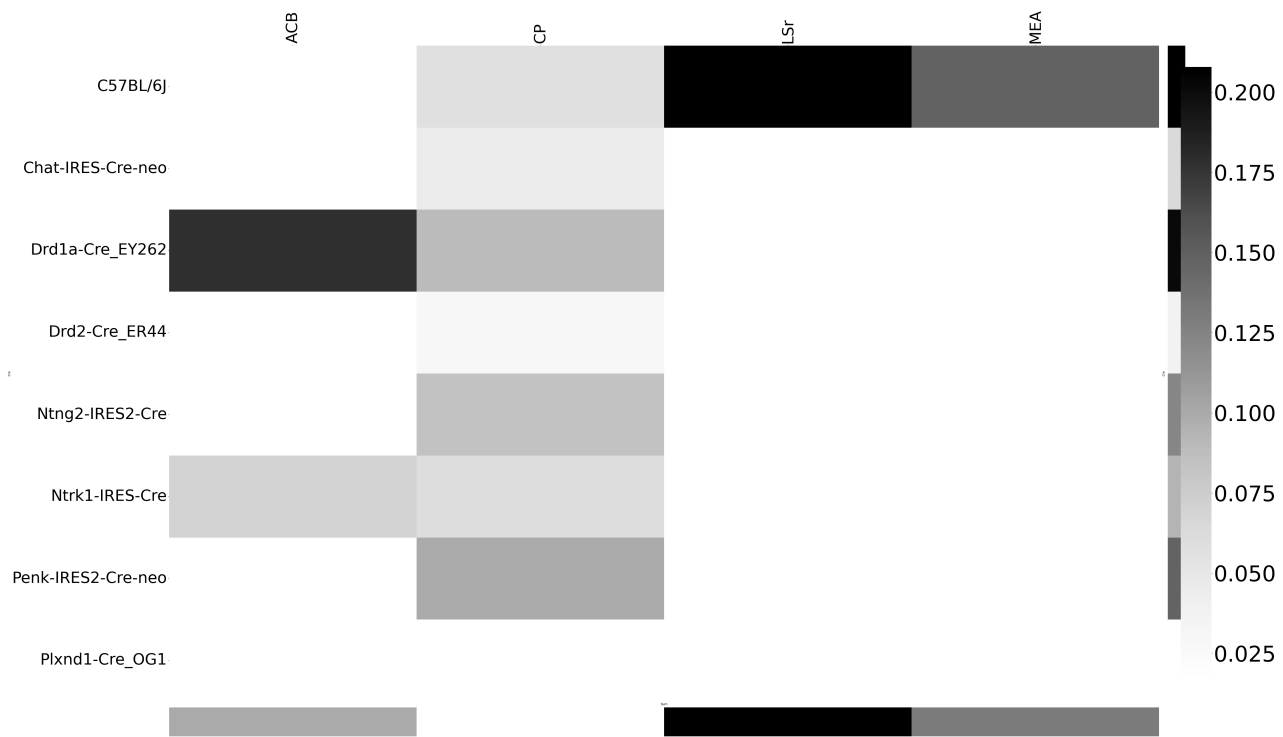


Figure 29: Weighted loss for cre-leaf combinations in STR. Missing values are omitted. Row and column averages are also plotted.

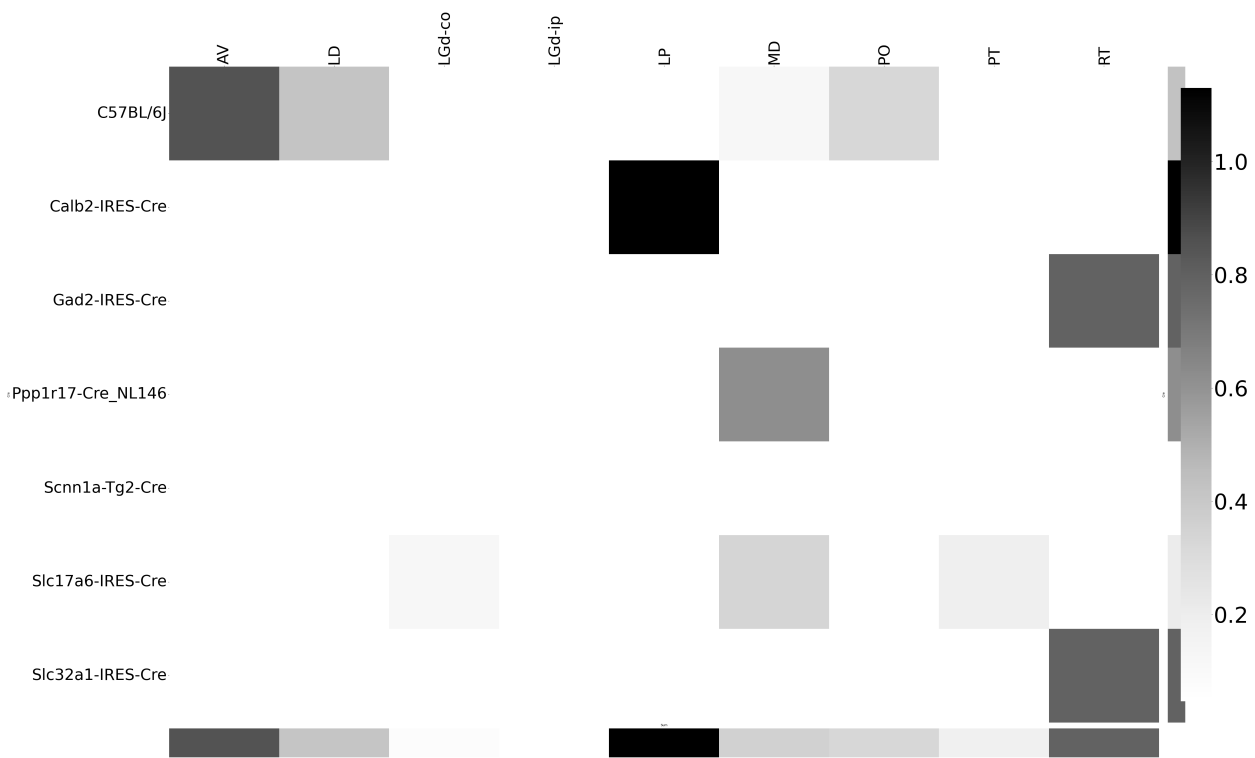


Figure 30: Weighted loss for cre-leaf combinations in TH. Missing values are omitted. Row and column averages are also plotted.

585 ***Matrix Factorization***

586 We give additional results on the generation of the archetypal connectome patterns. These consist of
 587 cross-validation selection of q , the number of latent components, stability analysis, and visualization
 588 of the reconstructed wild-type connectivity.

589 *Cross-validation* We set $\alpha = 0.002$ and run Program 2 on \mathcal{C}_{wt} . We use a random mask with $p = .3$ to
 590 evaluate prediction accuracy of models trained on the unmasked data on the masked data. To
 591 account for stochasticity in the NMF algorithm, we run $R = 8$ replicates at each potential dimension q .
 592 This selects $\hat{q} = 60$.

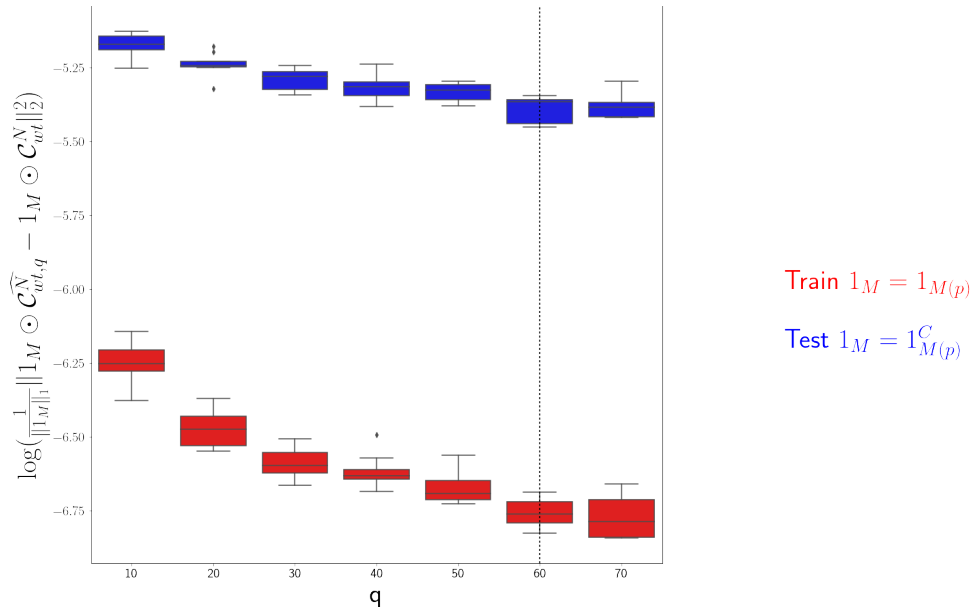


Figure 31: Train and test error using NMF decomposition.

593 *Stability* For the purposes of visualization and interpretability, we restrict to a $q = 15$ component
 594 model. To address the instability of the NMF algorithm in identifying components, we $k - \text{means}$
 595 cluster components over $R = 10$ replicates with $k \in \{10, 15, 20, 25, 30\}$. Since the clustering is itself
 596 unstable, we repeat the clustering 25 times and select the k with the largest Rand index.

597 q	10.000000	20.000000	30.000000	40.000000	50.000000	
	Rand index	0.772544	0.844981	0.932957	0.929827	0.885862

598 Since k -means is most stable at $k = 30$, we cluster the $qR = 150$ components into 30 clusters and
 599 select the 15 clusters appearing in the most replicates.

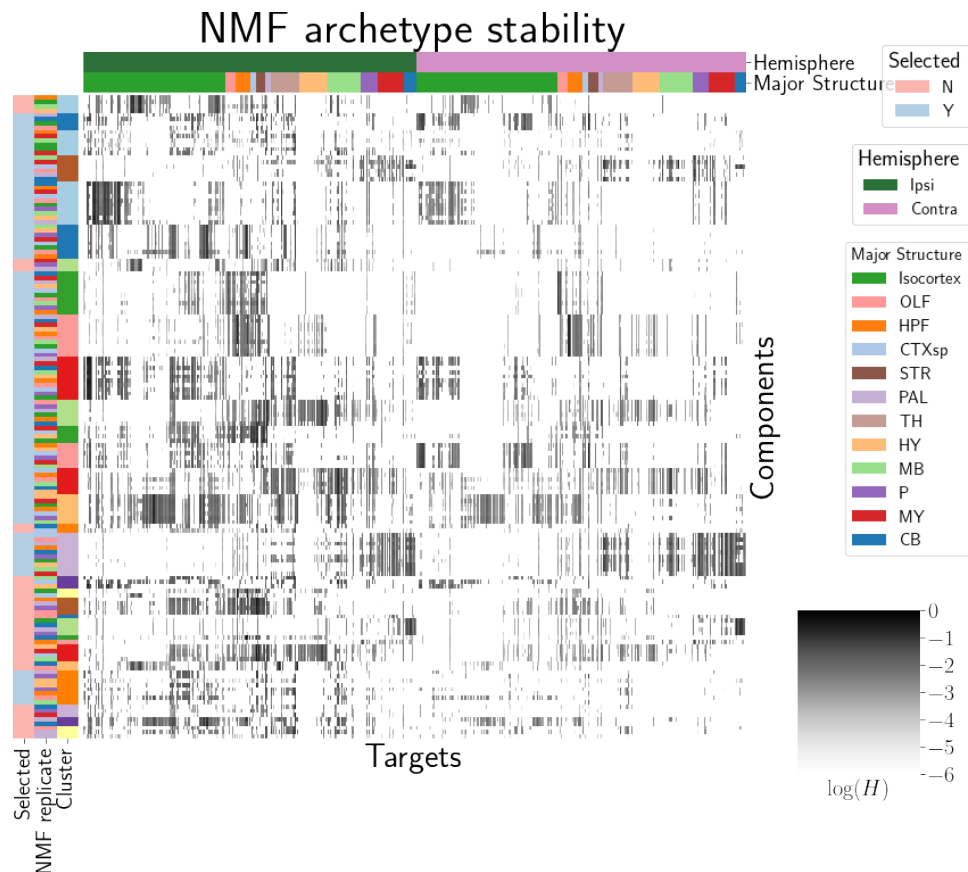


Figure 32: Stability of NMF results across replicates. Replicate and NMF component are shown on rows. Components that are in the top 15 are also indicated.

600 These are the components whose medians are plotted in Figure 4a.

8 COMPETING INTERESTS

- 601 This is an optional section. If you declared a conflict of interest when you submitted your manuscript,
602 please use this space to provide details about this conflict.

603

604

REFERENCES

605

606 Brunet, J.-P., Tamayo, P., Golub, T. R., & Mesirov, J. P. (2004). Metagenes and molecular pattern discovery using matrix
607 factorization. *Proc. Natl. Acad. Sci. U. S. A.*, 101(12), 4164–4169.

608 Chamberlin, N. L., Du, B., de Lacalle, S., & Saper, C. B. (1998). Recombinant adeno-associated virus vector: use for
609 transgene expression and anterograde tract tracing in the CNS. *Brain Res.*, 793(1-2), 169–175.

610 Daigle, T. L., Madisen, L., Hage, T. A., Valley, M. T., Knoblich, U., Larsen, R. S., ... Zeng, H. (2018). A suite of transgenic
611 driver and reporter mouse lines with enhanced Brain-Cell-Type targeting and functionality. *Cell*, 174(2), 465–480.e22.

612 Gao, Y., Zhang, X., Wang, S., & Zou, G. (2016). Model averaging based on leave-subject-out cross-validation. *J. Econom.*,
613 192(1), 139–151.

614 Harris, J. A., Mihalas, S., Hirokawa, K. E., Whitesell, J. D., Choi, H., Bernard, A., ... Zeng, H. (2019). Hierarchical
615 organization of cortical and thalamic connectivity. *Nature*, 575(7781), 195–202.

616 Harris, J. A., Oh, S. W., & Zeng, H. (2012). Adeno-associated viral vectors for anterograde axonal tracing with fluorescent
617 proteins in nontransgenic and cre driver mice. *Curr. Protoc. Neurosci., Chapter 1, Unit 1.20.1–18*.

618 Harris, K. D., Mihalas, S., & Shea-Brown, E. (2016). Nonnegative spline regression of incomplete tracing data reveals high
619 resolution neural connectivity.

620 Huang, K. W., Ochandarena, N. E., Philson, A. C., Hyun, M., Birnbaum, J. E., Cicconet, M., & Sabatini, B. L. (2019).
621 Molecular and anatomical organization of the dorsal raphe nucleus. *Elife*, 8.

622 Jeong, M., Kim, Y., Kim, J., Ferrante, D. D., Mitra, P. P., Osten, P., & Kim, D. (2016). Comparative three-dimensional
623 connectome map of motor cortical projections in the mouse brain. *Sci. Rep.*, 6, 20072.

624 Knox, J. E., Harris, K. D., Graddis, N., Whitesell, J. D., Zeng, H., Harris, J. A., ... Mihalas, S. (2019). High-resolution
625 data-driven model of the mouse connectome. *Netw Neurosci*, 3(1), 217–236.

626 Kotliar, D., Veres, A., Nagy, M. A., Tabrizi, S., Hodis, E., Melton, D. A., & Sabeti, P. C. (2019). Identifying gene expression
627 programs of cell-type identity and cellular activity with single-cell RNA-Seq. *Elife*, 8.

- 628 Li, X., Yu, B., Sun, Q., Zhang, Y., Ren, M., Zhang, X., ... Qiu, Z. (2018). Generation of a whole-brain atlas for the
 629 cholinergic system and mesoscopic projectome analysis of basal forebrain cholinergic neurons. *Proc. Natl. Acad. Sci.*
 630 *U. S. A.*, 115(2), 415–420.
- 631 Lotfollahi, M., Naghipourfar, M., Theis, F. J., & Alexander Wolf, F. (2019). Conditional out-of-sample generation for
 632 unpaired data using trVAE.
- 633 Muzerelle, A., Scotto-Lomassese, S., Bernard, J. F., Soiza-Reilly, M., & Gaspar, P. (2016). Conditional anterograde tracing
 634 reveals distinct targeting of individual serotonin cell groups (B5-B9) to the forebrain and brainstem. *Brain Struct.*
 635 *Funct.*, 221(1), 535–561.
- 636 Oh, S. W., Harris, J. A., Ng, L., Winslow, B., Cain, N., Mihalas, S., ... Zeng, H. (2014). A mesoscale connectome of the
 637 mouse brain. *Nature*, 508(7495), 207–214.
- 638 Ren, J., Friedmann, D., Xiong, J., Liu, C. D., Ferguson, B. R., Weerakkody, T., ... Luo, L. (2018). Anatomically defined and
 639 functionally distinct dorsal raphe serotonin sub-systems. *Cell*, 175(2), 472–487.e20.
- 640 Ren, J., Isakova, A., Friedmann, D., Zeng, J., Grutzner, S. M., Pun, A., ... Luo, L. (2019). Single-cell transcriptomes and
 641 whole-brain projections of serotonin neurons in the mouse dorsal and median raphe nuclei. *Elife*, 8.
- 642 Saul, L. K., & Roweis, S. T. (2003). Think globally, fit locally: Unsupervised learning of low dimensional manifolds. *J.*
 643 *Mach. Learn. Res.*, 4(Jun), 119–155.
- 644 Servén D., B. C. (n.d.). *pygam: Generalized additive models in python*.
- 645 von Luxburg, U. (2010a). Clustering stability: An overview.
- 646 von Luxburg, U. (2010b). Clustering stability: An overview.
- 647 Watson, C., Paxinos, G., & Puelles, L. (2012). The mouse nervous system..
- 648 Wu, S., Joseph, A., Hammonds, A. S., Celiker, S. E., Yu, B., & Frise, E. (2016). Stability-driven nonnegative matrix
 649 factorization to interpret spatial gene expression and build local gene networks. *Proc. Natl. Acad. Sci. U. S. A.*, 113(16),
 650 4290–4295.
- 651 Zaborszky, L., Csordas, A., Mosca, K., Kim, J., Gielow, M. R., Vadasz, C., & Nadasdy, Z. (2015). Neurons in the basal
 652 forebrain project to the cortex in a complex topographic organization that reflects corticocortical connectivity

653 patterns: an experimental study based on retrograde tracing and 3D reconstruction. *Cereb. Cortex*, 25(1), 118–137.

9 TECHNICAL TERMS

654 **Technical Term** a key term that is mentioned in an NETN article and whose usage and definition may
655 not be familiar across the broad readership of the journal.

656 **Cre-line** Refers to the combination of cre-recombinase expression in transgenic mouse and
657 cre-induced promotion in the vector that induces labelling of cell-class specific projection.

658 **Cell class** The projecting neurons targeted by a particular cre-line

659 **Structural connectivities** connectivity between structures

660 **Voxel** A $100\mu m$ cube of brain.

661 **Structural connection tensor** Connectivities between structures given a neuron class

662 **dictionary-learning** A family of algorithms for finding low-dimensional data representations.

663 **Shape constrained estimator** A statistical estimator that fits a function of a particular shape (e.g.
664 monotonic increasing, convex).

665 **Nadaraya-Watson** A simple smoothing estimator.

666 **Connectivity archetypes** Typical connectivity patterns

667 **Expected loss** Our new estimator that weights different features by their estimated predictive
668 power.